



Contents lists available at ScienceDirect

## International Journal of Solids and Structures

journal homepage: [www.elsevier.com/locate/ijsolstr](http://www.elsevier.com/locate/ijsolstr)

# Poroelastic response of spherical indentation into a half space with a drained surface via step displacement

Ming Liu, Haiying Huang\*

School of Civil and Environmental Engineering, Georgia Institute of Technology, Atlanta, GA 30332, United States

## ARTICLE INFO

### Article history:

Received 9 September 2018

Revised 17 January 2019

Available online xxx

### Keywords:

Spherical indentation

Poroelasticity

Step displacement loading

Force relaxation curve

## ABSTRACT

Indentation of a poroelastic solid by a spherical-tip tool is analyzed within the framework of Biot's theory. We seek the response of the indentation force and the field quantities as functions of time when a rigid pervious indenter is loaded instantaneously to a fixed depth. The particular case where the surface of the semi-infinite domain is permeable and under a drained condition is considered. Compressibility of both the fluid and solid phases is taken into account. The solution procedure based on the McNamee-Gibson displacement function method is adopted in this work. One of the difficulties in solving poroelastic contact problems theoretically is in evaluating integrals with kernels that oscillate rapidly. We show that such issues can be overcome by using alternative integral representations with exponentially decaying functions in the kernels. Special functions, such as the modified Struve functions and the modified Bessel functions, and the method of contour integration can be utilized to aid the removal of the oscillation. Problem formulation and the solution procedure are first introduced. Implications of the poroelastic solution for incipient failure in form of tensile crack initiation and onset of plastic deformation are then discussed. An interesting outcome from this analysis is that the transient response of the dimensionless indentation force shows only weak dependence on one derived material constant and can in fact be fitted by a simple elementary function, which can then be conveniently used for material characterization in the laboratory.

© 2019 Published by Elsevier Ltd.

## 1. Introduction

The process of indentation by a rigid tool has been widely studied for its versatility as an experimental technique to probe constitutive properties of materials of various kinds across multiple scales (Cook and Pharr, 1990; Lawn, 1998; Marshall et al., 2015; Argatov and Mishuris, 2018). Recently, spherical indentation has been applied to characterize poroelasticity of fully saturated porous media such as polymeric gels and hydrated bones via either displacement- or force-controlled tests. In a displacement-controlled load relaxation test, the indenter is pressed instantaneously to a fixed depth and held until the indentation force approaches a horizontal asymptote (Hu et al., 2010; 2011a; 2011b; 2012; Kalciglu et al., 2012), whereas in a step force loading or ramp-hold test, the indentation force is kept constant after reaching a prescribed level (Oyen, 2008; Galli and Oyen, 2008; 2009). In theory, for a step loading test, if both the solid and fluid phases can be considered incompressible, elastic constants can be determined from the early and late time responses, while the hydraulic

diffusivity can be obtained from the transient response by matching the measured indentation force or displacement as a function of time against a master curve. Such master curves for various indenter shapes have been previously constructed through finite element simulations (Hui et al., 2006; Lin and Hu, 2006; Lin et al., 2007; Galli and Oyen, 2009; Hu et al., 2010; 2011a; 2011b; Lai and Hu, 2017) and also semi-analytically for spherical indentation with step force loading (Agbezuge and Deresiewicz, 1974). In general, after the indentation force or displacement is normalized by the early and late time asymptotes, these master curves can be fitted by rather simple functions.

Possibility of using spherical indentation to determine the hydraulic diffusivity was first suggested by Agbezuge and Deresiewicz (1974). They outlined theoretical treatment for indentation with a rigid sphere subjected to a constant force for three distinct surface drainage conditions, namely, case I of a permeable indenter on a permeable half space, case II of an impermeable indenter on a permeable half space and case III of an impermeable indenter on a permeable half space. In the literature, only a few additional cases of poroelastic contact problems have been investigated theoretically and their primary focus was on ground settlement caused by surface loading. In the earlier work, the constituents are treated as

\* Corresponding author.

E-mail address: [haiying.huang@ce.gatech.edu](mailto:haiying.huang@ce.gatech.edu) (H. Huang).

incompressible. Among them, McNamee and Gibson (1960b) considered uniform mechanical loading along an infinite strip and over a circular area, respectively. Chiarella and Booker (1975) investigated the contact with a rigid cylindrical punch. Deresiewicz (1979) analyzed uniform circular loading on a partially permeable surface. Compressibility of both the fluid and solid phases was considered by Verruijt (2013) for uniform loading over a circular area, by Yue and Selvadurai for a cylindrical punch subjected to a constant force (Yue and Selvadurai, 1995) and by Lan and Selvadurai for interaction between two cylindrical punches (Lan and Selvadurai, 1996).

Methods of solution for this class of problems can be classified into two groups (Kim and Selvadurai, 2016). The approach in Chiarella and Booker (1975), Yue and Selvadurai (1995) and Lan and Selvadurai (1996) first expresses field quantities using integral transform representations of unknown functions, which then need to satisfy a system of ordinary differential equations. On the other hand, the McNamee–Gibson displacement function method (McNamee and Gibson, 1960a) used in McNamee and Gibson (1960b), Agbezuge and Deresiewicz (1974), Deresiewicz (1979), Verruijt (2013) and Kim and Selvadurai (2016) first reduces the governing equations to canonical forms by introducing two scalar functions. Field quantities are then expressed as partial derivatives of these two functions. Uniqueness of the solution is therefore ensured. Though the two methods provide general solution procedures, one of the mathematical difficulties is in evaluating integrals with kernels that oscillate rapidly.

In this work, we show that such issues can in fact be overcome by using alternative integral representations with exponentially decaying functions in the kernels. Special functions, such as the modified Struve functions and the modified Bessel functions, and the method of contour integration can be utilized to aid the removal of the oscillation. These techniques are applied here to solve poroelastic spherical indentation within the framework of Biot's theory (Biot, 1941; Rice and Cleary, 1976; Detournay and Cheng, 1993). Specifically, we use the McNamee–Gibson displacement function method to consider the case where a rigid smooth sphere is subjected to step displacement loading and the surface drainage condition is case I as defined in Agbezuge and Deresiewicz (1974).

Compressibility of both the fluid and solid phases is taken into account in our analysis. Constituent compressibility is particularly important when dealing with poroelastic response of geological materials such as rocks, where the bulk modulus of the solid phase could be comparable with that of the skeleton. Poroelastic characterization of rocks is crucial to the analyses of many geological processes and subsurface engineering applications in the fields of geomechanics, hydrogeology, and reservoir engineering (Wang, 2000). In addition, in drilling, the action of a single bit in a drill bit pressing normally against a rock surface causing the rock underneath the bit to crush and fracture is essentially an indentation process (Fowell, 1993; Cook et al., 1984). Insights into the poroelastic effect on the indentation process could potentially help predict and improve the drilling efficiency.

This paper is organized by first introducing the problem formulation and solution procedure. Derivation to obtain the poroelastic fields is then shown. Implications of the poroelastic solution for incipient failure in form of tensile crack initiation and onset of plastic deformation are also discussed. Though derivation of this fully coupled poroelastic solution requires the aid of a variety of mathematical techniques, the result in terms of the normalized indentation force relaxation with time is remarkably simple and shows only weak dependence on one derived material constant. Master curves of the normalized transient force response can be constructed by fitting the theoretical solution using a simple elementary function, which then lends itself to convenient use for material characterization in the laboratory.

## 2. Problem formulation

### 2.1. Governing equations

Governing equations for an axisymmetric fully poroelastic problem in a half space ( $z \geq 0$ ) can be written using the displacement functions  $\mathcal{D}$  and  $\mathcal{F}$  (McNamee and Gibson, 1960a; Verruijt, 2013), which satisfy,

$$\frac{\partial}{\partial t} \nabla^2 \mathcal{D} = c \nabla^2 \nabla^2 \mathcal{D} \quad (1)$$

$$\nabla^2 \mathcal{F} = 0 \quad (2)$$

where,

$$\nabla^2 = \frac{\partial^2}{\partial r^2} + \frac{1}{r} \frac{\partial}{\partial r} + \frac{\partial^2}{\partial z^2} \quad (3)$$

$$c = \frac{\kappa(K + \frac{4}{3}G)}{[\alpha^2 + S(K + \frac{4}{3}G)]\mu} \quad (4)$$

$$\alpha = 1 - \frac{K}{K_s} \quad (5)$$

$$S = \frac{n}{K_f} + \frac{\alpha - n}{K_s} \quad (6)$$

The linear poroelastic response is described by the following list of independent material constants:  $\kappa$  – permeability,  $\mu$  – fluid viscosity,  $K$  – skeleton bulk modulus,  $G$  – skeleton shear modulus,  $n$  – porosity,  $K_f$  – fluid bulk modulus,  $K_s$  – solid bulk modulus. In addition to the diffusion coefficient,  $c$ , the Biot coefficient,  $\alpha$ , and the storage coefficient,  $S$ , two other derived material constants,  $\eta$  and  $\phi$ , are defined to facilitate the derivation,

$$\eta = \frac{K}{2G} + \frac{2}{3} \quad (7)$$

$$\phi = \frac{\alpha^2 + S(K + \frac{4}{3}G)}{\alpha^2 + S(K + \frac{1}{3}G)} \quad (8)$$

Pore pressure, stresses and displacements can be directly expressed using displacement functions  $\mathcal{D}$  and  $\mathcal{F}$ ,

$$\frac{\alpha p}{2G} = -\eta \nabla^2 \mathcal{D} + [\phi + 2\eta(1 - \phi)] \frac{\partial \mathcal{F}}{\partial z} \quad (9)$$

$$\frac{\sigma_z}{2G} = -\nabla^2 \mathcal{D} + \frac{\partial^2 \mathcal{D}}{\partial z^2} - z \frac{\partial^2 \mathcal{F}}{\partial z^2} + \phi \frac{\partial \mathcal{F}}{\partial z} \quad (10)$$

$$\frac{\sigma_r}{2G} = -\nabla^2 \mathcal{D} + \frac{\partial^2 \mathcal{D}}{\partial r^2} - z \frac{\partial^2 \mathcal{F}}{\partial r^2} + (2 - \phi) \frac{\partial \mathcal{F}}{\partial z} \quad (11)$$

$$\frac{\sigma_\theta}{2G} = -\nabla^2 \mathcal{D} + \frac{1}{r} \frac{\partial \mathcal{D}}{\partial r} - \frac{z}{r} \frac{\partial \mathcal{F}}{\partial r} + (2 - \phi) \frac{\partial \mathcal{F}}{\partial z} \quad (12)$$

$$\frac{\sigma_{zr}}{2G} = \frac{\partial^2 \mathcal{D}}{\partial r \partial z} - z \frac{\partial^2 \mathcal{F}}{\partial r \partial z} - (1 - \phi) \frac{\partial \mathcal{F}}{\partial r} \quad (13)$$

$$u_z = -\frac{\partial \mathcal{D}}{\partial z} + z \frac{\partial \mathcal{F}}{\partial z} + (1 - 2\phi)\mathcal{F} \quad (14)$$

$$u_r = -\frac{\partial \mathcal{D}}{\partial r} + z \frac{\partial \mathcal{F}}{\partial r} \quad (15)$$

where  $p$  is the pore pressure;  $\sigma_z$ ,  $\sigma_r$ ,  $\sigma_\theta$ ,  $\sigma_{zr}$  are the non-trivial stress components;  $u_z$  and  $u_r$  are the vertical and radial displacements. Compression positive is adopted for the sign convention.

**Table 1**  
Boundary conditions.

Time domain	Laplace domain
$0 \leq r \leq a_-$	$u_z = \left(d - \frac{r^2}{2R}\right) \mathbb{H}(t)$
$\sigma_{zr} = p = 0$	$\bar{u}_z = s^{-1} \left(d - \frac{r^2}{2R}\right)$
$r \geq a_+$	$\sigma_z = \sigma_{zr} = p = 0$
	$\bar{\sigma}_z = \bar{\sigma}_{zr} = \bar{p} = 0$

General solutions for Eqs. (1) and (2) can be obtained from Hankel transform in the Laplace domain. After neglecting the terms unbounded at infinity, we obtain,

$$\bar{D} = \int_0^\infty \left[ A_1(s, \xi) \exp(-z\xi) + A_2(s, \xi) \exp\left(-z\sqrt{\xi^2 + \lambda}\right) \right] J_0(r\xi) d\xi \quad (16)$$

$$\bar{F} = \int_0^\infty B_1(s, \xi) \exp(-z\xi) J_0(r\xi) d\xi \quad (17)$$

where  $\lambda = s/c$  and  $s$  is the Laplace variable;  $J_\nu(\cdot)$  is the Bessel function of the first kind of order  $\nu$ ;  $A_1$ ,  $A_2$  and  $B_1$  are functions of  $s$  and  $\xi$  to be determined from the boundary conditions. The overbar is used here to denote the functions in the Laplace domain.

## 2.2. Boundary conditions

Heaviside step displacement loading is applied to the spherical-tip indenter. Conformity can be assumed at the frictionless contact surface. It follows from the classical Hertzian solution (Love, 1929; Johnson, 1987; Liu and Huang, 2016) that when the domain is fully undrained ( $t = 0$ ) or drained ( $t \rightarrow \infty$ ), the contact radius  $a$  at these two limits can be determined from  $a = \sqrt{Rd}$ , where  $d$  is the depth of penetration and  $R$  is the radius of the indenter. For the transient period, an assumption about the contact radius needs to be made. It was argued in Agbezuge and Deresiewicz (1974) and Hu et al. (2010) that since the relation for  $a$ ,  $d$  and  $R$  is purely geometrical at the two limits, it is reasonable to hypothesize that  $a = \sqrt{Rd}$  still holds at  $t > 0$ . This assumption is also adopted in our analysis in order to make the problem amenable to mathematical treatment. Implications of such an assumption will be discussed later in Section 5.3. Boundary conditions can now be written in terms of vertical displacement  $u_z$ , stresses  $\sigma_z$  and  $\sigma_{zr}$ , and pore pressure  $p$  on the surface, see Table 1, where  $\mathbb{H}(t)$  is the Heaviside step function.

Matching the poroelastic fields with the boundary conditions in the Laplace domain yields the following equations,

$$A_1\xi + A_2\sqrt{\xi^2 + \lambda} + B_1(1 - \phi) = 0 \quad (18)$$

$$A_2\eta\lambda + B_1\xi[\phi + 2\eta(1 - \phi)] = 0 \quad (19)$$

and a dual integral equation containing only the unknown  $B_1$ ,

$$\int_0^\infty B_1 J_0(r\xi) d\xi = (s\phi)^{-1} \left( \frac{r^2}{2R} - d \right), \quad 0 \leq r \leq a_- \quad (20)$$

$$\int_0^\infty [1 + \omega H(s, \xi)] \xi B_1 J_0(r\xi) d\xi = 0, \quad r \geq a_+ \quad (21)$$

where,

$$H(s, \xi) = 1 + 2\lambda^{-1}\xi^2 - 2\lambda^{-1}\xi\sqrt{\xi^2 + \lambda} \quad (22)$$

$$\omega = \frac{\phi + 2\eta(1 - \phi)}{\phi(2\eta - 1)} \quad (23)$$

The problem now reduces to first finding  $B_1$  through Eqs. (20)–(21) and then  $A_1$  and  $A_2$  from Eqs. (18)–(19).

**Table 2**  
A list of poroelastic materials from Cheng (2016) and their  $\omega$  values.

Material	$\omega$	Material	$\omega$
1 Ruhr sandstone	0.2544	9 Boise sandstone	0.1792
2 Tennessee marble	0.0213	10 Gulf of Mexico shale	0.4174
3 Charcoal granite	0.0308	11 Danian chalk	0.2019
4 Berea sandstone	0.1637	12 hard sediment	0.4904
5 Westerly granite	0.1206	13 soft sediment	0.4881
6 Weber sandstone	0.1665	14 Abyssal red clay	0.0036
7 Ohio sandstone	0.1372	15 rock salt	0.0322
8 Pecos sandstone	0.2156	16 coarse sand	0.3333

Constant  $\omega$  can be expressed explicitly using other material constants,

$$\omega = \alpha^2(1 - 2\nu) \left( \alpha^2 + 2SG \frac{1 - \nu}{1 - 2\nu} \right)^{-1} \quad (24)$$

where  $\nu$  is the drained Poisson's ratio. Since  $0 \leq \alpha \leq 1$ ,  $S \geq 0$ ,  $G \geq 0$  and  $0 \leq \nu \leq 0.5$ , the theoretical range of  $\omega$  is  $[0, 1]$ . If both the fluid and solid phases are incompressible,  $\omega$  becomes a function of  $\nu$  only,  $\omega = 1 - 2\nu$ .

Based on the material constants listed in Cheng (2016), the values of  $\omega$  for sixteen saturated poroelastic media appear to fall within the range between 0 and 0.5, see Table 2. The saturating fluid is kerosene for Boise sandstone (No. 9) and salt water for Abyssal red clay (No. 14). All the others are saturated in water. For the saturated hydrogel in Hu et al. (2010),  $\omega = 0.44$ .

## 3. Fredholm integral equation of the second kind

Noble (1963) showed that the pair of dual integral equations in Eqs. (20)–(21) can be reduced to a Fredholm integral equation of the second kind. By applying the following Sonine's integrals to Eqs. (20)–(21), respectively,

$$\xi^{-\frac{1}{2}} J_{\frac{1}{2}}(x\xi) = \sqrt{\frac{2}{\pi}} x^{-\frac{1}{2}} \int_0^x J_0(r\xi) r (x^2 - r^2)^{-\frac{1}{2}} dr \quad (25)$$

$$\xi^{-\frac{1}{2}} J_{-\frac{1}{2}}(x\xi) = \sqrt{\frac{2}{\pi}} x^{-\frac{1}{2}} \int_x^\infty J_0(r\xi) r (r^2 - x^2)^{-\frac{1}{2}} dr \quad (26)$$

we obtain,

$$\int_0^\infty B_1 \xi^{-\frac{1}{2}} J_{\frac{1}{2}}(x\xi) d\xi = \sqrt{\frac{2}{\pi}} (s\phi)^{-1} x^{-\frac{1}{2}} \left( \frac{x^3}{3R} - xd \right), \quad 0 \leq x \leq a_- \quad (27)$$

and,

$$\int_0^\infty [1 + \omega H(s, \xi)] B_1 \xi^{\frac{1}{2}} J_{-\frac{1}{2}}(x\xi) d\xi = 0, \quad x \geq a_+ \quad (28)$$

In order to make the orders of the Bessel functions and the powers of  $\xi$  identical in the above equations, both sides of Eq. (27) are first multiplied by  $x^{\frac{1}{2}}$  and then differentiated with respect to  $x$ ,

$$\int_0^\infty B_1 \xi^{\frac{1}{2}} J_{-\frac{1}{2}}(x\xi) d\xi = \sqrt{\frac{2}{\pi}} (s\phi)^{-1} x^{-\frac{1}{2}} \left( \frac{x^2}{R} - d \right), \quad 0 \leq x \leq a_- \quad (29)$$

Define  $\theta(s, x)$  as an unknown function of  $s$  and  $x$  in the Laplace domain according to,

$$\int_0^\infty B_1 \xi^{\frac{1}{2}} J_{-\frac{1}{2}}(x\xi) d\xi = \sqrt{\frac{2}{\pi}} (s\phi)^{-1} \frac{\theta(s, x)}{R}, \quad x \geq a_+ \quad (30)$$

Since the left hand sides of Eqs. (29) and (30) are identical, the expression on the left is defined for all  $x$ . It follows from inverse

Hankel transform,

$$B_1 \xi^{-\frac{1}{2}} = \sqrt{\frac{2}{\pi}} (s\phi)^{-1} \int_0^a m^{\frac{1}{2}} \left( \frac{m^2}{R} - d \right) J_{-\frac{1}{2}}(m\xi) dm + \sqrt{\frac{2}{\pi}} (s\phi)^{-1} \int_a^\infty \left( \frac{m}{R} \right) \theta(s, m) J_{-\frac{1}{2}}(m\xi) dm \quad (31)$$

Substituting Eq. (31) into Eq. (28) gives a Fredholm integral equation of the second kind for  $\theta(s, x)$ ,

$$\theta(s, x) + \omega \int_a^\infty \left[ m \int_0^\infty \xi H(s, \xi) J_{-\frac{1}{2}}(x\xi) J_{-\frac{1}{2}}(m\xi) d\xi \right] \theta(s, m) dm = \omega \int_0^a m^{-\frac{1}{2}} (Rd - m^2) \left[ m \int_0^\infty \xi H(s, \xi) J_{-\frac{1}{2}}(x\xi) J_{-\frac{1}{2}}(m\xi) d\xi \right] dm \quad (32)$$

Eq. (32) extends the definition of  $\theta(s, x)$  from  $x \geq a_+$  to  $x \geq 0$ .

For convenience, the following dimensionless variables are introduced,

$$x_* = x/a \quad m_* = m/a \quad r_* = r/a \quad z_* = z/a \\ \xi_* = \xi/a \quad s_* = \lambda a^2 \quad t_* = tc/a^2$$

Denote function  $\theta_1(s_*, x_*)$  as the normalized  $\theta(s, x)$  according to,

$$\theta_1(s_*, x_*) = \theta(s, x) a^{-\frac{3}{2}}$$

Eq. (32) can be rewritten as,

$$\theta_1(s_*, x_*) + \omega \int_1^\infty N(s_*, x_*, m_*) \theta_1(s_*, m_*) dm_* = \omega M(s_*, x_*) \quad (33)$$

where,

$$N(s_*, x_*, m_*) = m_* \int_0^\infty \xi_* H_1(s_*, \xi_*) J_{-\frac{1}{2}}(x_* \xi_*) J_{-\frac{1}{2}}(m_* \xi_*) d\xi_* \quad (34)$$

$$M(s_*, x_*) = \int_0^1 m_*^{-\frac{1}{2}} (1 - m_*^2) N(s_*, x_*, m_*) dm_* \quad (35)$$

$$H_1(s_*, \xi_*) = 1 + 2s_*^{-1} \xi_*^2 - 2s_*^{-1} \xi_* (\xi_*^2 + s_*)^{\frac{1}{2}} \quad (36)$$

Now  $\theta_1(s_*, x_*)$  is the unknown to be determined. Once it is known, all the field quantities can be expressed in the Laplace domain in terms of  $\theta_1(s_*, x_*)$ . It is noted that  $\theta_1(s_*, x_*)$  is influenced by the material properties only through  $\omega$ .

Prior to finding the solution to Eq. (33), function  $N(s_*, x_*, m_*)$  needs to be evaluated. Methodologies for evaluating  $N(s_*, x_*, m_*)$  and then  $M(s_*, x_*)$  and  $\theta_1(s_*, x_*)$  are outlined next.

## 4. Solution methodology

### 4.1. Alternative Expression for $N(s_*, x_*, m_*)$

Though uniformly convergent,  $N(s_*, x_*, m_*)$  in Eq. (34) has an oscillatory integral kernel over an unbounded interval. As  $x_*$  and  $m_*$  become large, the rapidly oscillating integrand could result in unstable numerical integration. Yue and Selvadurai (1995) separated the integrand into two parts so that one deals with its asymptote as  $s_*^{-1} \xi_*^2 \rightarrow \infty$ , the integral of which can be expressed in closed form, and the other is the difference between the integrand and its asymptote, which reduces to zero relatively faster and thus can be numerically treated more effectively. Lan and Selvadurai (1996) used a function to fit  $H_1(s_*, \xi_*)$ . The fitting function is chosen in such a way that a closed form solution can be obtained for  $N(s_*, x_*, m_*)$ .

In this study, we take a different approach by expressing  $N(s_*, x_*, m_*)$  using an alternative integral expression. Indeed,  $N(s_*, x_*, m_*)$  can be rewritten using one of the integral representations of

the modified Struve functions (Olver et al., 2010), in which the oscillatory nature is no longer present. Since  $J_{-\frac{1}{2}}(y) = \sqrt{2/\pi} y \cos y$ ,  $N(s_*, x_*, m_*)$  can be rewritten as,

$$N(s_*, x_*, m_*) = \frac{1}{\pi} \left( \frac{m_*}{x_*} \right)^{\frac{1}{2}} \int_0^\infty H_1(s_*, \xi_*) \left[ \cos(x_* \xi_* - m_* \xi_*) + \cos(x_* \xi_* + m_* \xi_*) \right] d\xi_* \quad (37)$$

Integration by parts three times on the right hand side (RHS) of Eq. (37) gives,

$$\text{RHS} = \frac{2}{\pi} \left( \frac{m_*}{x_*} \right)^{\frac{1}{2}} \left\{ (x_* - m_*)^{-2} \left[ s_*^{-\frac{1}{2}} - \frac{3s_*}{x_* - m_*} \int_0^\infty (\xi_*^2 + s_*)^{-\frac{5}{2}} \times \sin[(x_* - m_*) \xi_*] d\xi_* \right] + (x_* + m_*)^{-2} \times \left[ s_*^{-\frac{1}{2}} - \frac{3s_*}{x_* + m_*} \int_0^\infty (\xi_*^2 + s_*)^{-\frac{5}{2}} \sin[(x_* + m_*) \xi_*] d\xi_* \right] \right\} \quad (38)$$

Though the integrals in Eq. (38) still contain oscillatory terms, the integrals are related to the modified Struve function through,

$$\int_0^\infty (\xi_*^2 + s_*)^{-\frac{5}{2}} \sin(y \xi_*) d\xi_* = -\frac{\pi}{6} y |s_*|^{-1} M_{-2}(|y| s_*^{\frac{1}{2}}) \quad (39)$$

where  $M_\nu(\cdot)$  is the modified Struve function of the second kind of order  $\nu$ . According to Olver et al. (2010), Eq. (39) holds, provided that  $|y| s_*^{\frac{1}{2}} \geq 0$ . This requirement is fulfilled since  $|y| \geq 0$  and  $s_* \geq 0$  in the Stehfest algorithm (Stehfest, 1970) for the inverse Laplace transform.

According to the recurrence relationship for the modified Struve function, we have

$$M_{-2}(y) = M_0(y) - 2y^{-1} M_1(y) - \frac{2}{\pi} y^{-1} \quad (40)$$

Functions  $M_0(y)$  and  $M_1(y)$  can be expressed through integral representations that do not contain oscillatory terms,

$$M_0(y) = -\frac{2}{\pi} \int_0^1 \exp(-y\zeta) (1 - \zeta^2)^{-\frac{1}{2}} d\zeta \quad (41)$$

$$M_1(y) = -\frac{2}{\pi} y \int_0^1 \exp(-y\zeta) (1 - \zeta^2)^{\frac{1}{2}} d\zeta \quad (42)$$

The integrals in Eqs. (41) and (42) have an exponentially decaying function in the kernels and a finite integral upper limit, and thus can be numerically integrated efficiently and effectively.

In addition, we can use the asymptotic behaviors of  $M_0(y)$  and  $M_1(y)$  for approximation, if the numerical integration cannot return satisfactory results at small or large  $y$ , e.g.,

$$\lim_{y \rightarrow 0} M_0(y) = -1 + \frac{2}{\pi} y - \frac{1}{4} y^2 + \frac{2}{9\pi} y^3 \quad (43)$$

$$\lim_{y \rightarrow \infty} M_0(y) = -\frac{2}{\pi} y^{-1} - \frac{2}{\pi} y^{-3} - \frac{18}{\pi} y^{-5} \quad (44)$$

$$\lim_{y \rightarrow 0} M_1(y) = -\frac{1}{2} y + \frac{2}{3\pi} y^2 - \frac{1}{16} y^3 \quad (45)$$

$$\lim_{y \rightarrow \infty} M_1(y) = -\frac{2}{\pi} + \frac{2}{\pi} y^{-2} + \frac{6}{\pi} y^{-4} \quad (46)$$

It follows from Eqs. (38)–(42) that an alternative expression for  $N(s_*, x_*, m_*)$  can be written as,



$$N(s_*, x_*, m_*) = \left(\frac{s_* m_*}{x_*}\right)^{\frac{1}{2}} \left\{ y_1^{-1} \left[ M_0(y_1) - \frac{2M_1(y_1)}{y_1} \right] + y_2^{-1} \left[ M_0(y_2) - \frac{2M_1(y_2)}{y_2} \right] \right\}$$

$$y_1 = |x_* - m_*| s_*^{\frac{1}{2}} \quad y_2 = (x_* + m_*) s_*^{\frac{1}{2}} \quad (47)$$

Some asymptotic expressions of  $N(s_*, x_*, m_*)$  are straightforward to obtain,

$$\lim_{s_* \rightarrow \infty} N(s_*, x_*, m_*) = \delta(m_* - x_*) \quad (48)$$

$$\lim_{s_* \rightarrow 0} N(s_*, x_*, m_*) = 0 \quad (49)$$

$$\lim_{x_* \rightarrow \infty} N(s_*, x_*, m_*) = \frac{4}{\pi} \left(\frac{m_*}{s_*}\right)^{\frac{1}{2}} x_*^{-\frac{5}{2}} \quad (50)$$

Comparison between direct numerical integration of Eq. (37) with the oscillatory kernel and the alternative expression in Eq. (47) at  $x_* = 1$ ,  $s_* = 5,000$  and  $s_* = 500,000$  are shown in Fig. 1. The results in both cases are obtained by directly using the “integral” command in MATLAB®. Direct integration of Eq. (37) yields highly oscillatory results at large  $s_*$  (small  $t_*$ ) and fails to capture the Dirac function behavior at  $m_* = x_*$ , which is expected for  $N(s_*, x_*, m_*)$  at large  $s_*$  according to Eq. (48). In contrast, the alternative expression with the modified Struve functions is well behaved and approaches  $\delta(m_* - x_*)$  at large  $s_*$ .

Using the alternative expression for  $N(s_*, x_*, m_*)$ , a closed form solution for  $M(s_*, x_*)$  consisting of special functions such as the hypergeometric functions can be obtained. However, the exact expression of  $M(s_*, x_*)$  is cumbersome and barely offers any advantage over direct numerical evaluation of Eq. (35) in terms of computational speed and accuracy. Indeed, as long as sufficient integration points are added in the vicinity of the peak in  $N(s_*, x_*, m_*)$ , direct numerical integration to determine  $M(s_*, x_*)$  is rather efficient. The relative error from direct numerical integration is smaller than  $10^{-5}$  in this study.

#### 4.2. Successive substitution

To solve for  $\theta_1(s_*, x_*)$  in Eq. (33), we adopt the method of successive substitution (Zemlyan, 2012) by letting,

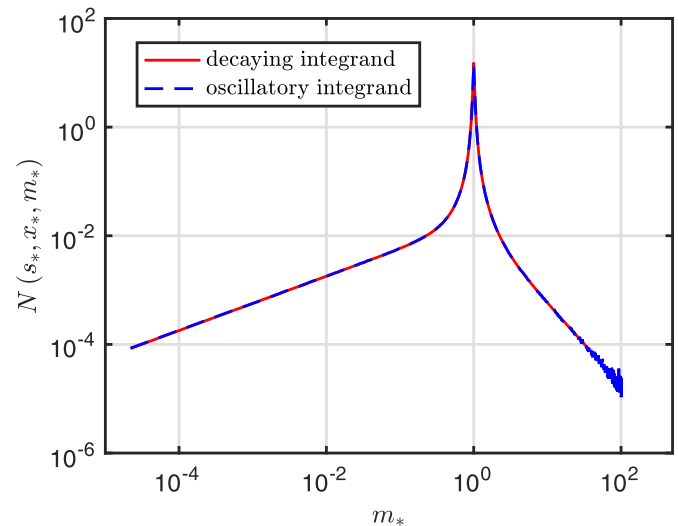
$$\theta_1(s_*, x_*) = - \sum_{n=0}^{\infty} (-\omega)^{n+1} a_n(s_*, x_*) \quad (51)$$

where,

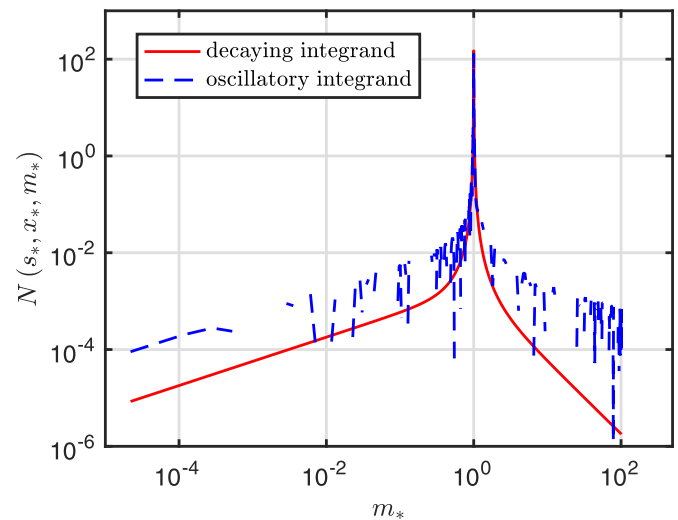
$$a_0(s_*, x_*) = M(s_*, x_*) \quad (52)$$

$$a_n(s_*, x_*) = \int_1^{\infty} N(s_*, x_*, m_*) a_{n-1}(s_*, m_*) dm_* \quad n = 1, 2, 3... \quad (53)$$

Numerical integration for the improper integral in Eq. (53) is performed by substituting its infinite upper bound with a sufficiently large value (say, 100), and assigning adequate integration points in the vicinity of the peak in  $N(s_*, x_*, m_*)$ . Summation of the infinite series is also replaced by a partial sum. It is observed that when  $\omega \leq 0.5$  as in the cases for the porous media in Table 2, the series converges rather fast and the partial sum with only 20 terms is sufficient to give a satisfactory approximation for any values of  $s_*$  and  $x_*$ . For example, when  $s_* = 500,000$  and  $\omega = 0.25$ , at  $x_* = 1$ ,  $a_n$  decreases with the increase of  $n$  and the largest term is  $a_0 = 0.01$ . This means that the largest truncation error of the partial sum with 20 terms is  $0.01 \sum_{n=21}^{\infty} \omega^n \approx 3 \times 10^{-15}$ , much smaller than  $\theta_1 = 0.00232$  at  $x_* = 1$ .



(a)  $s_* = 5,000$



(b)  $s_* = 500,000$

**Fig. 1.** Comparison between direct numerical integration of the oscillatory kernel and the alternative expression with the modified Struve functions for  $N(s_*, x_*, m_*)$  at  $x_* = 1$ .

By substituting Eq. (50) into Eqs. (33) and (35), the asymptotes of  $\theta_1(s_*, x_*)$  and  $M(s_*, x_*)$  at  $x_* \rightarrow \infty$  can be expressed explicitly,

$$\lim_{x_* \rightarrow \infty} \log[\theta_1(s_*, x_*)] = -\frac{5}{2} \log(x_*) + C_1 \quad (54)$$

$$\lim_{x_* \rightarrow \infty} \log[M(s_*, x_*)] = -\frac{5}{2} \log(x_*) + C_2 \quad (55)$$

where  $C_1$  and  $C_2$  are constants and equal to,

$$C_1 = \log \left[ \frac{4\omega}{\pi} s_*^{-\frac{1}{2}} \left( \frac{2}{3} - \int_1^{\infty} m_*^{\frac{1}{2}} \theta_1(s_*, m_*) dm_* \right) \right] \quad (56)$$

$$C_2 = \log \left( \frac{8}{3\pi} s_*^{-\frac{1}{2}} \right) \quad (57)$$

The limits of  $\theta_1(s_*, x_*)$  at  $s_* \rightarrow 0$  and  $s_* \rightarrow \infty$  can be determined after substituting Eqs. (48) and (49) into Eq. (33),

$$\lim_{s_* \rightarrow \infty} \theta_1(s_*, x_*) = \omega x_*^{-\frac{1}{2}} (1 - x_*^2), \quad 0 \leq x_* \leq 1$$

$$\lim_{s_* \rightarrow \infty} \theta_1(s_*, x_*) = 0, \quad x_* \geq 1 \quad (58)$$

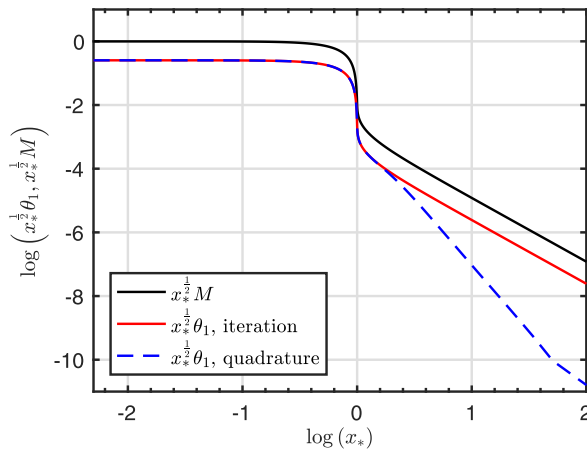


**Fig. 2.** Comparison between the method of successive substitution ('iteration') and the method of quadrature for  $\theta_1(s^*, x^*)$  at  $s^* = 500,000$  and  $\omega = 0.25$ .

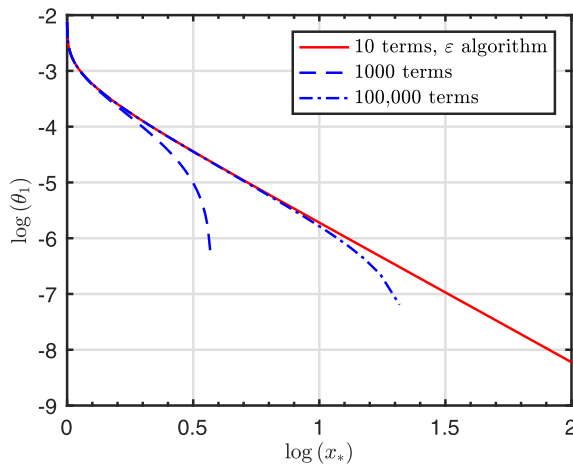


**Fig. 3.** Comparison between the partial sum results with 1,000 and 100,000 terms and the accelerated result using the  $\epsilon$ -algorithm for  $\theta_1(s^*, x^*)$  for  $\omega = 1$  and  $s^* = 500,000$ .

$$\lim_{s^* \rightarrow 0} \theta_1(s^*, x^*) = 0, \quad x^* \geq 0 \quad (59)$$

A comparison between the method of successive substitution and the method of quadrature for determining  $\theta_1(s^*, x^*)$  is shown in Fig. 2 for  $s^* = 500,000$  and  $\omega = 0.25$ . The method of quadrature was previously used in the literature (Agbezuge and Deresiewicz, 1974; Chiarella and Booker, 1975; Yue and Selvadurai, 1995; Lan and Selvadurai, 1996). Though the difference between the results from the two approaches is not significant in a linear scale, the method of successive substitution is able to recover the analytical asymptote of  $\theta_1(s^*, x^*)$  at large  $x^*$ . As indicated by Eqs. (54) and (55), when  $x^* \rightarrow \infty$ ,  $\theta_1(s^*, x^*)$  and  $M(s^*, x^*)$  should be parallel to each other with a slope of  $-5/2$  in the log-log scale. The deficiency in the quadrature method is likely due to the fact that the information around the peak of  $N(s^*, x^*, m^*)$  when  $x^*$  is large is not adequately captured.

Theoretically, the value of  $\omega$  could be close or equal to 1. In that case, the alternating series in Eq. (51) converges slowly. Wynn's epsilon algorithm (Wynn, 1956) is employed here to accelerate the convergence for the method's effectiveness in dealing with an alternating series. Fig. 3 presents a comparison between the accelerated result using the  $\epsilon$ -algorithm based on the first 10 terms in the series only and the partial sum results with 1,000 and 100,000 terms for  $\omega = 1$  and  $s^* = 500,000$ . It shows that the accelerated

result is well behaved and acts like an upper bound for the results from the partial sum.

## 5. Poroelastic fields

Poroelastic fields on the surface and inside the half space can now be expressed in terms of  $\theta_1(s^*, x^*)$  in the Laplace domain by directly substituting the displacement functions  $\bar{\mathcal{D}}$  and  $\bar{\mathcal{F}}$  into Eqs. (11)–(15). However, these expressions from direct substitution all contain integrals with oscillatory kernels. As will be shown later in Section 5.1, direct evaluation of these integrals could yield non-smooth results at small depth. As such, a second set of expressions is derived with the aid of Abel transform (Bracewell, 1986) and Sonine's integral (Noble, 1963). For the second set, the expressions for the surface and inside the half space are listed separately.

The pair of forward and inverse Abel transform used in this study is,

$$F(x) = 2 \int_x^\infty f(r) r (r^2 - x^2)^{-\frac{1}{2}} dr \quad (60)$$

$$f(r) = -\frac{1}{\pi} \int_r^\infty \frac{dF(x)}{dx} (x^2 - r^2)^{-\frac{1}{2}} dx \quad (61)$$

The inverse transform in Eq. (61) is applicable only if  $F(x)$  is continuous. Generalization to account for discontinuity in  $F(x)$ , for example, at  $x = 1$ ,  $F(x_-) - F(x_+) = C$  where  $C$  is a constant, can be expressed as,

$$f(r) = -\frac{1}{\pi} \int_r^\infty \frac{d[F(x) - C\mathbb{H}(1-x)]}{dx} (x^2 - r^2)^{-\frac{1}{2}} dx + \frac{C}{\pi} (1 - r^2)^{-\frac{1}{2}} \mathbb{H}(1-r) \quad (62)$$

The formula below, derived from Sonine's finite integral (Noble, 1963), will also be used,

$$\xi^{-\frac{1}{2}} J_{\frac{1}{2}}(x\xi) = \sqrt{\frac{2}{\pi}} x^{\frac{1}{2}} \int_x^\infty J_1(r\xi) (r^2 - x^2)^{-\frac{1}{2}} dr \quad (63)$$

In addition, two techniques are used to rewrite the integrals in the second set of expressions. The first one is to express the integrals alternatively using the modified Bessel functions of the second kind (Bateman, 1954), for example,

$$\int_0^\infty \exp(-z\sqrt{\xi^2 + s}) \cos(y\xi) d\xi = zs^{\frac{1}{2}} (y^2 + z^2)^{-\frac{1}{2}} K_1 \left[ s^{\frac{1}{2}} (y^2 + z^2)^{\frac{1}{2}} \right] \quad (64)$$

where  $K_1(\cdot)$  is the modified Bessel functions of the second kind of order 1. One of the integral representations of  $K_1(\cdot)$  does not contain an oscillatory kernel. The second technique is the method of contour integration, see details in Appendix B.

Poroelastic fields in the time domain can be obtained by using the Stehfest algorithm (Stehfest, 1970) for inverse Laplace transform with six expansion terms. Derivation of the pore pressure  $\bar{p}$ , vertical stress  $\bar{\sigma}_z$  and displacement  $\bar{u}_z$  is shown next. Details of the other non-trivial stresses and displacements are given in Appendix A. Their early and late time asymptotes, which correspond to the undrained and drained responses of the Hertzian contact, are given in Appendix A.5.

Material properties of the Gulf of Mexico shale as listed in Cheng (2016), see Table 3, are used for the subsequent calculation of the field quantities and the incipient failure analysis. Viscosity of the saturating fluid is taken to be  $\mu = 1$  cp. Values of the drained and undrained Poisson's ratios are  $\nu = 0.219$  and  $\nu_u = 0.449$ , which correspond to  $\omega = 0.4174$ . Radius of the spherical-tip indenter is taken as  $R = 50$  mm and the indentation depth  $d = 0.1$  mm and the corresponding contact radius is  $a = 2.23$  mm for this example case.

**Table 3**  
Material constants of the Gulf of Mexico shale  
(Cheng, 2016).

Skeleton shear modulus, $G$	0.76 GPa
Skeleton compression modulus, $K$	1.1 GPa
Solid compression modulus, $K_s$	34 GPa
Fluid compression modulus, $K_f$	2.25 GPa
Porosity, $n$	0.3
Permeability, $\kappa$	$1 \times 10^{-19} \text{ m}^2$

## 5.1. Pore pressure

### 5.1.1. Expression 1

Substituting Eqs. (16)–(19) and (31) into Eq. (9) gives,

$$\alpha \bar{p} = \frac{4\eta Ga^3}{c\phi R} \left[ s_*^{-1} \int_0^1 (m_*^2 - 1) N_p(s_*, r_*, m_*, z_*) dm_* + s_*^{-1} \int_1^\infty m_*^{\frac{1}{2}} \theta_1(s_*, m_*) N_p(s_*, r_*, m_*, z_*) dm_* \right] \quad (65)$$

where,

$$N_p(s_*, r_*, m_*, z_*) = \sqrt{\frac{2}{\pi}} m_*^{\frac{1}{2}} \int_0^\infty \xi_*^{\frac{3}{2}} \left[ \frac{\omega}{1+\omega} \exp(-z_* \sqrt{\xi_*^2 + s_*}) - \frac{\omega}{1+\omega} \exp(-z_* \xi_*) \right] J_{-\frac{1}{2}}(m_* \xi_*) J_0(r_* \xi_*) d\xi_* \quad (66)$$

### 5.1.2. Expression 2

An alternative expression for the pore pressure field can be derived by first applying Sonine's integral in Eq. (26) to Eq. (65),

$$\begin{aligned} & \int_{x_*}^\infty \alpha \bar{p} r_* (r_*^2 - x_*^2)^{-\frac{1}{2}} dr_* \\ &= \frac{4\eta Ga^3}{c\phi R} \left[ s_*^{-1} \int_0^1 (m_*^2 - 1) N_{px}(s_*, x_*, m_*, z_*) dm_* + s_*^{-1} \int_1^\infty m_*^{\frac{1}{2}} \theta_1(s_*, m_*) N_{px}(s_*, x_*, m_*, z_*) dm_* \right] \end{aligned} \quad (67)$$

where,

$$N_{px}(s_*, x_*, m_*, z_*) = \frac{2}{\pi} \int_0^\infty \left[ \frac{\omega}{1+\omega} \exp(-z_* \sqrt{\xi_*^2 + s_*}) - \frac{\omega}{1+\omega} \exp(-z_* \xi_*) \right] \cos(m_* \xi_*) \cos(x_* \xi_*) d\xi_* \quad (68)$$

Since the right hand side of Eq. (67) is continuous at  $x_* \geq 0$ , applying the inverse Abel transform in Eq. (61) gives,

$$\alpha \bar{p} = -\frac{8\eta Ga^3}{\pi c\phi R} \int_{r_*}^\infty \theta_p(s_*, x_*, z_*) (x_*^2 - r_*^2)^{-\frac{1}{2}} dx_* \quad (69)$$

where,

$$\begin{aligned} \theta_p(s_*, x_*, z_*) &= s_*^{-1} \int_0^1 (m_*^2 - 1) N_{px,x}(s_*, x_*, m_*, z_*) dm_* \\ &+ s_*^{-1} \int_1^\infty m_*^{\frac{1}{2}} \theta_1(s_*, m_*) N_{px,x}(s_*, x_*, m_*, z_*) dm_* \end{aligned} \quad (70)$$

and  $N_{px,x} = \partial N_{px} / \partial x_*$ ,

$$\begin{aligned} N_{px,x}(s_*, x_*, m_*, z_*) &= -\frac{2}{\pi} \int_0^\infty \xi_* \left[ \frac{\omega}{1+\omega} \exp(-z_* \sqrt{\xi_*^2 + s_*}) - \frac{\omega}{1+\omega} \exp(-z_* \xi_*) \right] \cos(m_* \xi_*) \sin(x_* \xi_*) d\xi_* \end{aligned} \quad (71)$$

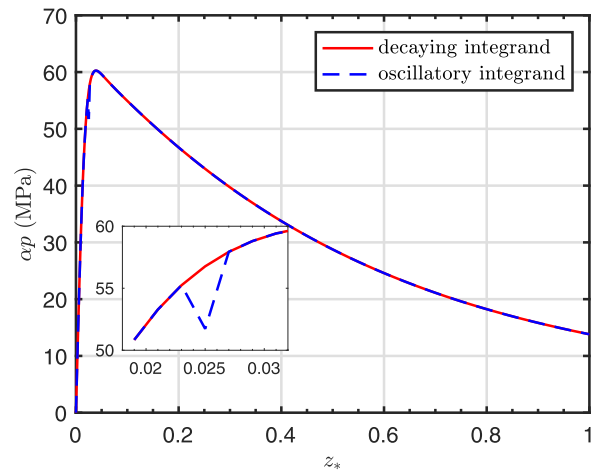


**Fig. 4.** Pore pressure along the contact axis at  $t_* = 10^{-4}$ ; evaluated based on Eq. (65) (solid line) and Eq. (69) (dashed line).

Here the first term in  $N_{px,x}$  can be evaluated with the aid of the modified Bessel function while the second term gives an elementary antiderivative.

Pore pressure in the time domain can be determined after taking the inverse Laplace transform. For example, for Eq. (69),

$$\alpha p = -\frac{8\eta Ga}{\pi \phi R} \int_{r_*}^\infty \mathcal{L}^{-1}[\theta_p(s_*, x_*, z_*)] (x_*^2 - r_*^2)^{-\frac{1}{2}} dx_* \quad (72)$$

Here  $\mathcal{L}^{-1}$  denotes the inverse Laplace transform with respect to  $s_*$ .

Both Eqs. (65) and (69) can be used to determine the pore pressure field inside the half space ( $z_* > 0$ ) in the Laplace domain. While it is easier to program with Eq. (65) in MATLAB®, the result from direct numerical integration at some depths when  $z_* < 0.05$  is not as smooth as that based on Eq. (69), see the inset in Fig. 4 showing the pore pressure distribution along the contact axis. The results are obtained with the properties of the Gulf of Mexico shale at  $t_* = 10^{-4}$ . The discrepancy at small  $z_*$  is because that as  $z_*$  becomes smaller, the oscillatory integrand in  $N_p$  approaches to zero slower than the decaying integrand in  $N_{px,x}$ . However, the two algorithms yield excellent agreement when  $z_* \geq 0.05$ .

There are benefits in having both sets of expressions. On the one hand, Eq. (65) has the advantage in calculating the pore pressure at a specific location when  $z_* \geq 0.05$  since the algorithm is less time consuming. On the other hand, Eq. (69) is more efficient in determining the full pore pressure field since once  $\theta_p$  is computed for all  $x_*$ , the pore pressure at any position can be conveniently calculated all at once.

Fig. 5 shows the pore pressure distributions along the contact axis at various times from Eq. (65) for  $z_* > 0.05$  and Eq. (69) for  $z_* \leq 0.05$ . Since a drained boundary is assumed, the pore pressure on the surface drops from the undrained asymptote to zero instantaneously. Along the contact axis, the pore pressure exhibits the Mandel-Cryer effect (Detournay and Cheng, 1993), where the pore pressure rises above the initial value at  $t_* = 0_+$  before its dissipation, see the inset in Fig. 5.

## 5.2. Vertical stress

### 5.2.1. Expression 1

The vertical stress field can be obtained after substituting Eqs. (16)–(19) and (31) into Eq. (10),

$$\begin{aligned} \bar{\sigma}_z &= \frac{2Ga^3}{c\phi R} \left[ s_*^{-1} \int_0^1 (m_*^2 - 1) N_{sz}(s_*, r_*, m_*, z_*) dm_* + s_*^{-1} \int_1^\infty m_*^{\frac{1}{2}} \theta_1(s_*, m_*) N_{sz}(s_*, r_*, m_*, z_*) dm_* \right] \end{aligned} \quad (73)$$

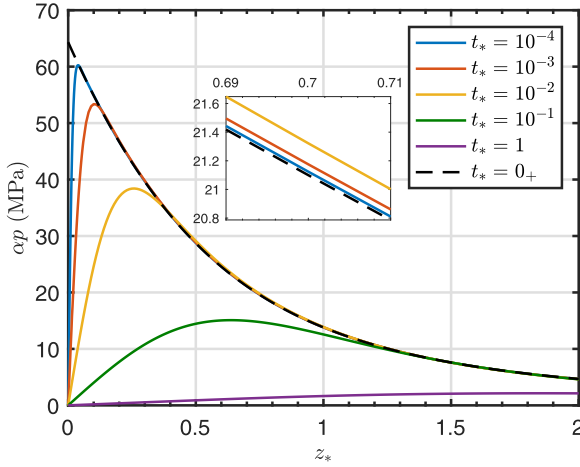


Fig. 5. Distribution of the pore pressure along the contact axis.

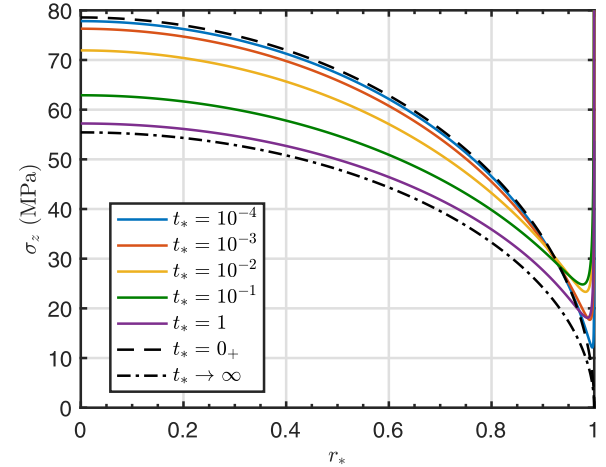


Fig. 6. Distribution of the contact pressure at various dimensionless times.

where,

$$N_{sz}(s_*, r_*, m_*, z_*) = \sqrt{\frac{2}{\pi}} m_*^{\frac{1}{2}} \int_0^{\xi_*} \xi_*^{\frac{3}{2}} \left[ \frac{2\omega}{1+\omega} s_*^{-1} \xi_* \sqrt{\xi_*^2 + s_*} \exp(-z_* \xi_*) - \frac{2\omega}{1+\omega} s_*^{-1} \xi_*^2 \exp(-z_* \sqrt{\xi_*^2 + s_*}) - (1 + z_* \xi_*) \exp(-z_* \xi_*) \right] J_{-\frac{1}{2}}(m_* \xi_*) J_0(r_* \xi_*) d\xi_* \quad (74)$$

### 5.2.2. Expression 2

Similar to the treatment for the pore pressure, an alternative expression for  $\bar{\sigma}_z$  can be obtained by first applying Eq. (26) to Eq. (73),

$$\begin{aligned} & \int_{x_*}^{\infty} \bar{\sigma}_z r_* (r_*^2 - x_*^2)^{-\frac{1}{2}} dr_* \\ &= \frac{2Ga^3}{c\phi R} \left[ s_*^{-1} \int_0^1 (m_*^2 - 1) N_{szx}(s_*, x_*, m_*, z_*) dm_* + s_*^{-1} \int_1^{\infty} m_*^{\frac{1}{2}} \theta_1(s_*, m_*) N_{szx}(s_*, x_*, m_*, z_*) dm_* \right] \end{aligned} \quad (75)$$

where,

$$N_{szx}(s_*, x_*, m_*, z_*) = \frac{2}{\pi} \int_0^{\xi_*} \left[ \frac{2\omega}{1+\omega} s_*^{-1} \xi_* \sqrt{\xi_*^2 + s_*} \exp(-z_* \xi_*) - \frac{2\omega}{1+\omega} s_*^{-1} \xi_*^2 \exp(-z_* \sqrt{\xi_*^2 + s_*}) - (1 + z_* \xi_*) \exp(-z_* \xi_*) \right] \cos(m_* \xi_*) \cos(x_* \xi_*) d\xi_* \quad (76)$$

Inside the half space ( $z_* > 0$ ), the vertical stress  $\bar{\sigma}_z$  is continuous at  $x_* \geq 0$ . Applying the inverse Abel transform in Eq. (61) to Eq. (75) gives,

$$\bar{\sigma}_z = -\frac{4Ga^3}{\pi c\phi R} \int_{r_*}^{\infty} \theta_{sz}(s_*, x_*, z_*) (x_*^2 - r_*^2)^{-\frac{1}{2}} dx_* \quad (77)$$

where,

$$\begin{aligned} \theta_{sz}(s_*, x_*, z_*) &= s_*^{-1} \int_0^1 (m_*^2 - 1) N_{szx}(s_*, x_*, m_*, z_*) dm_* \\ &+ s_*^{-1} \int_1^{\infty} m_*^{\frac{1}{2}} \theta_1(s_*, m_*) N_{szx}(s_*, x_*, m_*, z_*) dm_* \end{aligned} \quad (78)$$

and  $N_{szx,x} = \partial N_{szx} / \partial x_*$ ,

$$\begin{aligned} N_{szx,x}(s_*, x_*, m_*, z_*) &= -\frac{2}{\pi} \int_0^{\xi_*} \xi_*^{\frac{3}{2}} \left[ \frac{2\omega}{1+\omega} s_*^{-1} \xi_* \sqrt{\xi_*^2 + s_*} \exp(-z_* \xi_*) - \frac{2\omega}{1+\omega} s_*^{-1} \xi_*^2 \exp(-z_* \sqrt{\xi_*^2 + s_*}) - (1 + z_* \xi_*) \exp(-z_* \xi_*) \right] \cos(m_* \xi_*) \sin(x_* \xi_*) d\xi_* \end{aligned} \quad (79)$$

The first term in  $N_{szx,x}$  can be evaluated with the aid of the method of contour integration, see Appendix B. The second term can be expressed alternatively using the modified Bessel function. And the last term has an elementary antiderivative.

On the surface ( $z_* = 0$ ), the vertical stress  $\bar{\sigma}_z$  is non-trivial only when  $r_* \leq 1$ . Eq. (75) becomes,

$$\begin{aligned} & \int_{x_*}^{\infty} \bar{\sigma}_z r_* (r_*^2 - x_*^2)^{-\frac{1}{2}} dr_* \\ &= \frac{G(2\eta - 1)a^3}{c\eta R} s_*^{-1} \left[ \frac{1 - x_*^2}{+x_*^{\frac{1}{2}} \theta_1(s_*, x_*)} \right], \quad x_* \leq 1_- \end{aligned} \quad (80)$$

$$\int_{x_*}^{\infty} \bar{\sigma}_z r_* (r_*^2 - x_*^2)^{-\frac{1}{2}} dr_* = 0, \quad x_* \geq 1_+ \quad (81)$$

Since  $\theta_1(s_*, 1)$  is positive at  $s_* > 0$  (except  $s_* \rightarrow \infty$ ), the right hand side of Eq. (80) is nonzero at  $x_* = 1$ , suggesting that the integrals above are discontinuous at  $x_* = 1$ . Inverse Abel transform in Eq. (62) is therefore applied to Eqs. (80) and (81) to obtain the contact pressure,

$$\begin{aligned} \bar{\sigma}_z &= \frac{2G(2\eta - 1)a^3}{\pi c\eta R} s_*^{-1} \\ &\times \left[ \frac{2(1 - r_*^2)^{\frac{1}{2}} + \theta_1(s_*, 1)(1 - r_*^2)^{-\frac{1}{2}}}{-\int_{r_*}^1 \theta_3(s_*, x_*) (x_*^2 - r_*^2)^{-\frac{1}{2}} dx_*} \right], \quad r_* \leq 1 \end{aligned} \quad (82)$$

where,

$$\theta_3(s_*, x_*) = \frac{\partial}{\partial x_*} \left[ x_*^{\frac{1}{2}} \theta_1(s_*, x_*) \right] \quad (83)$$

The expression for evaluating  $\theta_3(s_*, x_*)$  is given in Appendix C.

Contact pressure for the example case is shown in Fig. 6. The contact pressure from the full poroelastic solution reduces to the classical Hertzian solution at  $t_* = 0_+$  and  $t_* \rightarrow \infty$ . At an intermediate time, the contact pressure is bounded by the two limits except near the contact edge around  $r_* = 1$ , where the contact pressure is in fact singular. Existence of such a singularity can be attributed to



the assumption of a fixed contact radius  $a$ . The underlying reason can be found in the transient response of the surface displacement in the next section.

### 5.3. Vertical displacement

#### 5.3.1. Expression 1

Vertical displacement  $\bar{u}_z$  can be obtained after substituting Eqs. (16)–(19) and (31) into Eq. (14),

$$\bar{u}_z = \frac{a^4}{c\phi R} \left[ s_*^{-1} \int_0^1 (m_*^2 - 1) N_{uz}(s_*, r_*, m_*, z_*) dm_* + s_*^{-1} \int_1^\infty m_*^{\frac{1}{2}} \theta_1(s_*, m_*) N_{uz}(s_*, r_*, m_*, z_*) dm_* \right] \quad (84)$$

where,

$$\begin{aligned} N_{uz}(s_*, r_*, m_*, z_*) &= \sqrt{\frac{2}{\pi}} m_*^{\frac{1}{2}} \int_0^\infty \xi_*^{\frac{1}{2}} \left\{ \frac{2\omega}{1+\omega} \left[ s_*^{-1} \xi_* \sqrt{\xi_*^2 + s_*} \exp(-z_* \xi_*) \right. \right. \\ &\quad \left. \left. - s_*^{-1} \xi_* \sqrt{\xi_*^2 + s_*} \exp\left(-z_* \sqrt{\xi_*^2 + s_*}\right) \right] \right. \\ &\quad \left. - (\phi + z_* \xi_*) \exp(-z_* \xi_*) \right\} J_{-\frac{1}{2}}(m_* \xi_*) J_0(r_* \xi_*) d\xi_* \end{aligned} \quad (85)$$

#### 5.3.2. Expression 2

Applying Eq. (26) to Eq. (84) gives,

$$\begin{aligned} \int_{x_*}^\infty \bar{u}_z r_* (r_*^2 - x_*^2)^{-\frac{1}{2}} dr_* &= \frac{a^4}{c\phi R} \left[ s_*^{-1} \int_0^1 (m_*^2 - 1) N_{uzx}(s_*, x_*, m_*, z_*) dm_* \right. \\ &\quad \left. + s_*^{-1} \int_1^\infty m_*^{\frac{1}{2}} \theta_1(s_*, m_*) N_{uzx}(s_*, x_*, m_*, z_*) dm_* \right] \end{aligned} \quad (86)$$

where,

$$\begin{aligned} N_{uzx}(s_*, x_*, m_*, z_*) &= \frac{2}{\pi} \int_0^\infty \xi_*^{-1} \left\{ \frac{2\omega}{1+\omega} \left[ s_*^{-1} \xi_* \sqrt{\xi_*^2 + s_*} \exp(-z_* \xi_*) \right. \right. \\ &\quad \left. \left. - s_*^{-1} \xi_* \sqrt{\xi_*^2 + s_*} \exp\left(-z_* \sqrt{\xi_*^2 + s_*}\right) \right] \right. \\ &\quad \left. - (\phi + z_* \xi_*) \exp(-z_* \xi_*) \right\} \cos(m_* \xi_*) \cos(x_* \xi_*) d\xi_* \end{aligned} \quad (87)$$

Inside the half space, applying Eq. (61) to Eq. (86) gives,

$$\bar{u}_z = -\frac{2a^4}{\pi c\phi R} \int_{r_*}^\infty \theta_{uz}(s_*, x_*, z_*) (x_*^2 - r_*^2)^{-\frac{1}{2}} dx_* \quad (88)$$

where,

$$\begin{aligned} \theta_{uz}(s_*, x_*, z_*) &= s_*^{-1} \int_0^1 (m_*^2 - 1) N_{uzx}(s_*, x_*, m_*, z_*) dm_* \\ &\quad + s_*^{-1} \int_1^\infty m_*^{\frac{1}{2}} \theta_1(s_*, m_*) N_{uzx}(s_*, x_*, m_*, z_*) dm_* \end{aligned} \quad (89)$$

and  $N_{uzx} = \partial N_{uz} / \partial x_*$ ,

$$\begin{aligned} N_{uzx}(s_*, x_*, m_*, z_*) &= -\frac{2}{\pi} \int_0^\infty \left\{ \frac{2\omega}{1+\omega} \left[ s_*^{-1} \xi_* \sqrt{\xi_*^2 + s_*} \exp(-z_* \xi_*) \right. \right. \\ &\quad \left. \left. - s_*^{-1} \xi_* \sqrt{\xi_*^2 + s_*} \exp\left(-z_* \sqrt{\xi_*^2 + s_*}\right) \right] \right. \\ &\quad \left. - (\phi + z_* \xi_*) \exp(-z_* \xi_*) \right\} \cos(m_* \xi_*) \sin(x_* \xi_*) d\xi_* \end{aligned} \quad (90)$$

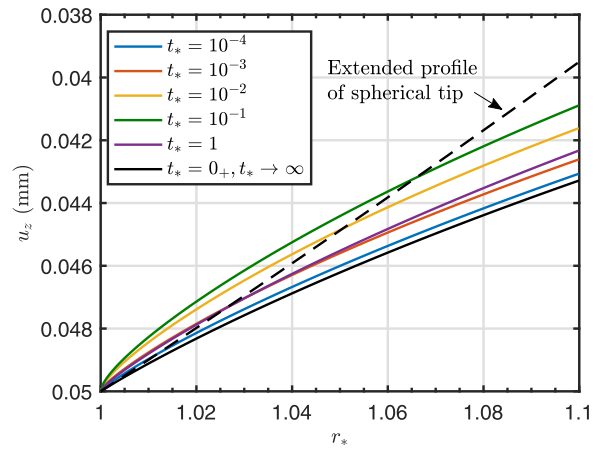


Fig. 7. Vertical displacement on the surface.

On the surface ( $z_* = 0$ ),  $N_{uz}$  can be expressed in a closed form,

$$N_{uz}(s_*, r_*, m_*, 0) = -\frac{2}{\pi} \phi (r_*^2 - m_*^2)^{-\frac{1}{2}} \mathbb{H}(r_* - m_*) \quad (91)$$

Substituting Eq. (91) into Eq. (84) gives,

$$\bar{u}_z = \frac{a^4}{cR} s_*^{-1} \left( 1 - \frac{1}{2} r_*^2 \right), \quad r_* \leq 1 \quad (92)$$

and,

$$\bar{u}_z = \frac{a^4}{\pi cR} s_*^{-1} \left[ (r_*^2 - 1)^{\frac{1}{2}} + (2 - r_*^2) \arcsin(r_*^{-1}) - 2 \int_1^{r_*} m_*^{\frac{1}{2}} \theta_1(s_*, m_*) (r_*^2 - m_*^2)^{-\frac{1}{2}} dm_* \right], \quad r_* \geq 1 \quad (93)$$

Vertical displacement on the surface outside of the contact area is shown in Fig. 7 for the example case. Vertical displacements at  $t_* = 0_+$  and  $t_* \rightarrow \infty$  are identical as they follow the Hertzian solution. At these two time limits, the deformed free surface is tangent to the indenter. Meanwhile, Fig. 7 shows that at a given radial distance  $r_*$ , variation of the downward displacement  $u_z$  with time is not monotonic. Among the seven time instances shown in Fig. 7,  $u_z$  first decreases with time when  $t_* \leq 0.1$ , but then increases after  $t_* > 0.1$ . The maximum is reached at  $t_* = 0_+$  and  $t_* \rightarrow \infty$ . In other words, after the instantaneous displacement (sink-in) at  $t_* = 0_+$ , the free surface outside of the contact region first rises when  $t_* \leq 0.1$ , but then subsides when  $t_* > 0.1$ . The upward relative displacement between  $t_* = 0_+$  and 0.1 would in fact be larger than the clearance between the deformed free surface at  $t_* = 0_+$  and the fixed indenter, if the spherical-tip indenter profile were to be extended beyond the prescribed contact edge at  $r_* = 1$ , see the dashed line in Fig. 7. Moreover, during the transient period, the free surface is no longer tangent to the indenter. Instead, there is a kink on the surface at  $r_* = 1$ .

These seemingly abnormal results are indeed direct consequence of the fixed contact radius assumption. Since only the geometry of the indenter tip in contact with the half space within  $r_* \leq 1$  is prescribed in the problem formulation, existence of the rigid tool at  $r_* > 1$  does not impose a constraint on the upward relative displacement of the free surface. Therefore, our theoretical solution is exact if the shape of the indenter above the initial contact area is such that the indenter does not get into contact with the deformed free surface at  $r_* > 1$  at any time. This would mean that the indenter has a corner at  $r_* = 1$ , which effectively allows a stress singularity to develop at the contact edge as shown in Fig. 6. On the other hand, if the indenter is simply a rigid sphere, our results indicate that the contact radius likely varies with time. The poroelastic effect can cause the contact edge to first gradually

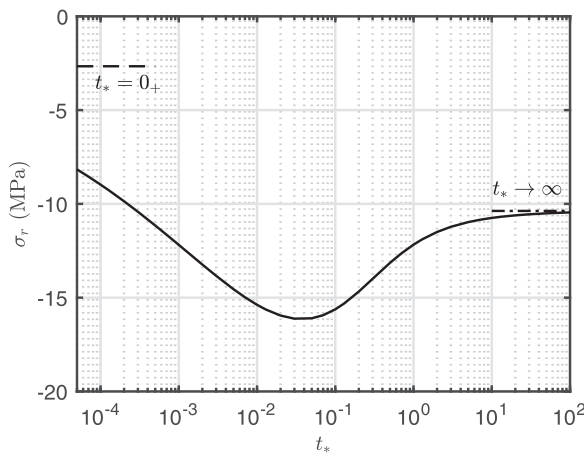


**Fig. 8.** Variation of the total/effective radial stress with the dimensionless time at  $r_* = 1_+$  on the surface (right outside of the contact area).

move outwards from its initial position at  $r_* = 1$ , but eventually recede back. Strictly speaking, this case of poroelastic indentation with a rigid sphere should be treated as a moving boundary problem. In that regard, our solution with the assumption of a fixed contact radius  $a$  is an approximation. We may argue that change in the contact radius with time is relatively small and the effect is negligible from a practical standpoint. Future work is needed to further explore this through numerical analysis where the assumption on the contact radius could be relaxed.

## 6. Incipient failure

Incipient failure in form of tensile fracturing and plastic deformation could take place in spherical indentation. It is therefore of interest to examine how poroelasticity could affect potential development of the indentation crack system and plastic failure. Biot's effective stress definition,  $\sigma'_{ij} = \sigma_{ij} - \alpha p$ , is adopted in the analysis below.

### 6.1. Cone crack initiation

The classical Hertzian cone crack initiates on the surface as a ring crack slightly outside of the contact area and propagates stably downwards to form a cone (Lawn, 1998). Since the pore pressure is zero on the surface in this problem, the effective stresses equal to the total stresses. As shown in Fig. 8, the total/effective radial stress at the contact edge ( $r_* = 1_+$ ) is always in tension. At  $t_* = 5 \times 10^{-5}$ ,  $\sigma_r = -8.16$  MPa. Magnitude of the radial stress then increases with time to reach its maximum,  $\sigma_r = -16.12$  MPa at  $t_* = 0.03$ . Eventually, the radial stress asymptotes to  $\sigma_r = -10.40$  MPa at late time. Since tensile strength of a shale is usually smaller than 10 MPa, a cone crack is very likely to occur in this case. In addition, the fact that the largest radial stress magnitude occurs at an intermediate time suggests that even if a cone crack does not initiate immediately when the indenter gets in contact with the porous medium, it may still appear after a certain time. However, it should be mentioned that these results should be understood with the fixed contact radius assumption in mind. How the tensile stress distribution will be affected by a moving contact boundary will need to be examined in future work.

### 6.2. Median crack initiation

According to the Hertzian solution, variation of the radial or tangential stress along the contact axis is not monotonic and the maximum tensile stress occurs beneath the surface. Theoretically, a

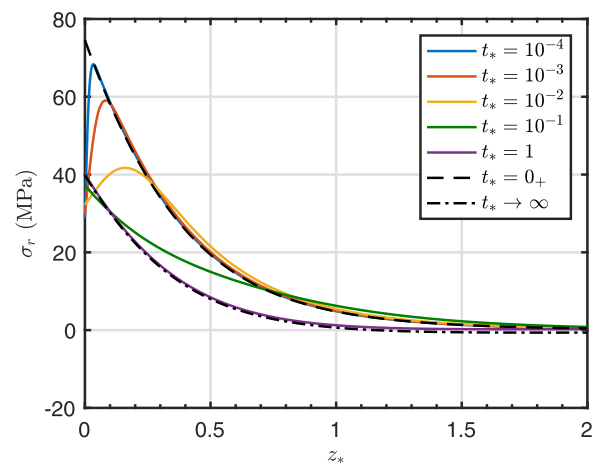


**Fig. 9.** Variation of the radial stress along the contact axis.

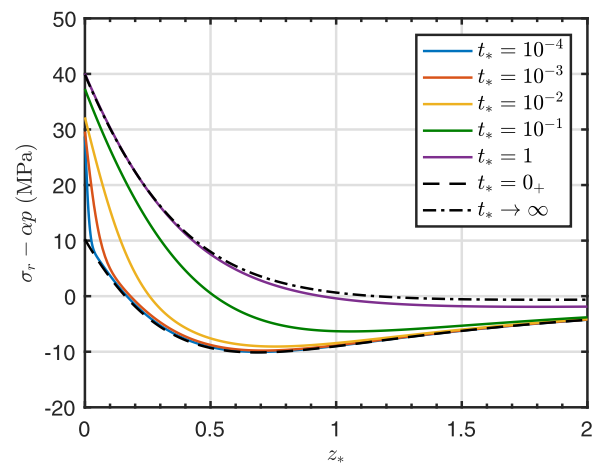


**Fig. 10.** Variation of the effective radial stress along the contact axis.

penny-shaped median crack may therefore nucleate from this location. For the Gulf of Mexico shale, with  $\nu_u = 0.449$  and  $\nu = 0.219$ , the classical Hertzian solution predicts the locations of the maximum tensile stress to be  $z_* = 4.76$  and  $1.83$ , which are consistent with our results at  $t_* = 0_+$  and  $\infty$ . Distribution of the total radial stress along the contact axis from the poroelastic solution is shown in Fig. 9. Since a drained boundary is assumed on the surface, the radial stress on the surface drops almost instantaneously from the undrained asymptote to a value slightly below the drained asymptote.

With the presence of excessive pore pressure inside the half space, at  $t_* = 0_+$ , the effective radial stress reaches a maximum in tension,  $\sigma'_r = -10.129$  MPa at  $z_* = 0.69$ , see Fig. 10. Compared with the maximum tension at  $t_* \rightarrow \infty$ , i.e.,  $\sigma'_r = -0.6423$  MPa at  $z_* = 1.83$ , the poroelastic effect results in a much larger tensile stress at a smaller depth. This means a median crack is more likely to be induced at an early time at a shallower position than predicted by the Hertzian solution with drained properties.

### 6.3. Onset of plastic deformation

At a given location, the maximum shear stress,  $(\sigma_z - \sigma_r)/2$ , can be used to infer the possibility of incipient plastic yielding. The Hertzian solution predicts plastic yielding to occur first only beneath the surface, see the dashed curves for  $t_* = 0_+$  and  $\infty$  in Fig. 11. However, the early time isochrones from the poroelastic solution reveal that the shear stress near the surface is in fact

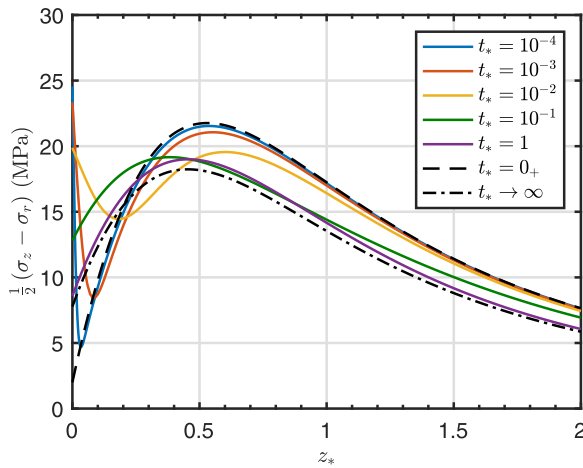


Fig. 11. Variation of the maximum shear stress along the contact axis.

comparable to the maxima around  $z_* = 0.5$  on the contact axis. This suggests that plastic deformation could take place almost instantaneously on the contact surface as well as inside the domain. However, it should be noted that in addition to the shear stress, failure for materials such as rocks could also depend on the effective mean stress. Since the effective mean stress is the most compressive right beneath the indenter, plastic deformation may not necessarily occur near the contact surface if the material behavior is governed by a pressure-sensitive failure criterion such as Mohr–Coulomb or Drucker–Prager.

## 7. Indentation force relaxation

The ratio between the early and late time asymptotes of the contact pressure (see A.5) can be expressed as,

$$\frac{\lim_{t \rightarrow 0} \sigma_z}{\lim_{t \rightarrow \infty} \sigma_z} \bigg|_{z_*=0} = \frac{2\eta}{(2\eta - 1)\phi} = 1 + \omega \quad (94)$$

Since the contact radius is assumed to remain fixed in this model, the ratio of the indentation forces at the early and late times is also,

$$\frac{F(0)}{F(\infty)} = 1 + \omega \quad (95)$$

where  $F(t)$  is the indentation force as a function of time. Indeed, integrating the normal stress over the contact area at  $t_* = 0_+$  and  $t \rightarrow \infty$ , the Hertzian solutions for the indentation force are recovered,

$$F(0) = \frac{16Ga^3}{3\phi R} \quad (96)$$

$$F(\infty) = \frac{8G(2\eta - 1)a^3}{3\eta R} \quad (97)$$

A normalized indentation force  $F_n(t_*)$  can be defined in a similar fashion to the degree of consolidation in Terzaghi's one-dimensional consolidation theory (Terzaghi, 1943), i.e.,

$$F_n(t_*) = \frac{F(t_*) - F(\infty)}{F(0) - F(\infty)} \quad (98)$$

where  $F_n(0) = 1$  and  $F_n(\infty) = 0$ . The explicit expression for  $F_n(t_*)$  is,

$$F_n(t_*) = \frac{3}{2\omega} \int_0^1 x_*^{\frac{1}{2}} \mathcal{L}^{-1}[s_*^{-1} \theta_1(s_*, x_*)] dx_* \quad (99)$$

Eq. (99) shows that the normalized transient force response is affected by material properties only through constant  $\omega$ . Moreover,

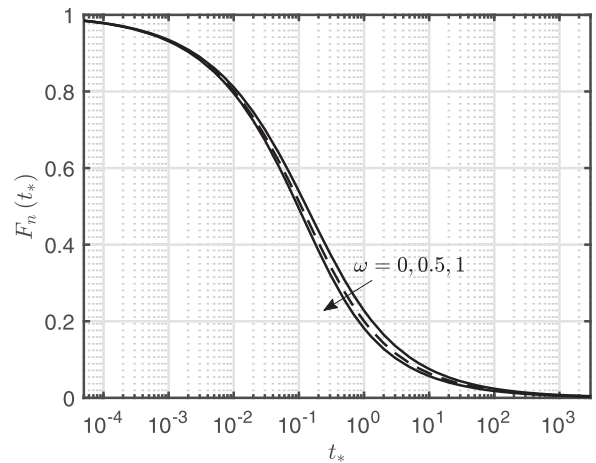


Fig. 12. Relaxation of the normalized indentation force with the dimensionless time.

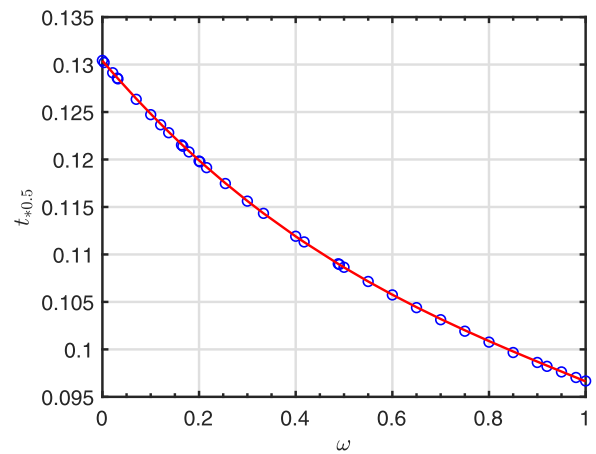
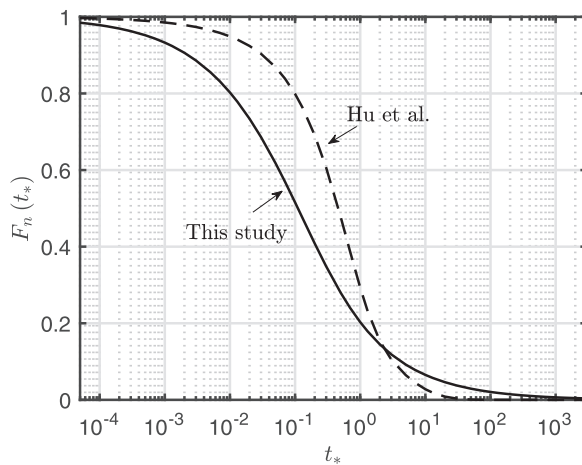


Fig. 13. Dimensionless time  $t_{0.5}$  as a function of  $\omega$ , fitted by  $t_{0.5} = 0.1304 - 0.05968\omega + 0.03869\omega^2 - 0.01278\omega^3$ .

as shown in Fig. 12, relaxation of the normalized indentation force does not appear to be very sensitive to  $\omega$ . Indeed, the dimensionless time  $t_{0.5}$  at which  $F_n(t_{0.5}) = 0.5$  varies only within a narrow range,  $t_{0.5} \in [0.0966, 0.1304]$  for  $\omega \in [0, 1]$ , see Fig. 13. In addition, it should be noted that though at  $\omega = 0$ , the indentation force remains constant and  $F_n(t_*)$  appears to become indefinite, mathematically, the limit of  $F_n(t_*)$  at  $\omega = 0$  exists and can still be calculated with our algorithms.

If the solid and fluid phases can be assumed as incompressible, we have  $\omega = 1 - 2\nu$ . The normalized force relaxation behavior is now affected by the Poisson's ratio only. Effect of the Poisson's ratio on the force relaxation response was previously observed in the numerical analysis of poroelastic indentation with a flat punch in plane strain (Bouklas et al., 2015). Nevertheless, the insensitivity to  $\omega$  shown in Fig. 12 signifies that the dependence of  $F_n(t_*)$  on  $\nu$  is rather weak. That could perhaps explain though the effect of the Poisson's ratio is not accounted for in the master curves constructed based on numerical analysis, e.g., Hu et al. (2010), those master curves still provide reliable interpretation for their experimental results.

A comparison between the result from this work and the fitting function,  $F_n(t_*) = 0.491 \exp(-0.908\sqrt{t_*}) + 0.509 \exp(-1.679t_*)$ , from the numerical analysis in Hu et al. (2010) suggests that effect of the surface drainage condition on the transient force response is appreciable, see Fig. 14. A drainage boundary condition of case III, where the surface is permeable only outside of the contact



**Fig. 14.** Comparison of the force relaxation curves between this study with  $\omega = 0.44$  and Hu et al. (2010).

**Table 4**  
Values of the fitting parameters for the force relaxation curves.

$\omega$	$a_1$	$b_1$	$a_2$	$b_2$
0	2.945	0.4636	3.906	0.733
0.1	3.013	0.4646	4.127	0.743
0.3	3.149	0.467	4.536	0.761
0.44	3.239	0.4686	4.801	0.773
0.5	3.278	0.4694	4.912	0.778
0.7	3.402	0.4718	5.262	0.793
0.9	3.52	0.474	5.589	0.806
1	3.58	0.4752	5.745	0.813

area, but impermeable within it, is imposed in Hu et al. (2010). This differs from the fully drained surface condition assumed in this model. Result from the present work with  $\omega = 0.44$  yields a smaller  $F_n(t_*)$  when  $t_* < 1$ . This means that the pore pressure dissipation response is faster in case I since the primary paths of fluid migration and consequently the characteristic relaxation time are shorter. However, at late time,  $F_n(t_*)$  from our solution approaches the zero asymptote slower. It is unclear to us whether that is because the numerical analysis in Hu et al. (2010) is performed with a finite model size or because of the discrepancy between the numerical results and the fitting function itself in Hu et al. (2010).

The force relaxation response from our theoretical solution, see Fig. 12, can be fitted by a four-parameter function  $f_n(t_*)$ ,

$$f_n(t_*) = \frac{1}{2} \left( \frac{1}{1 + a_1 t_*^{b_1}} + \frac{1}{1 + a_2 t_*^{b_2}} \right) \quad (100)$$

The fitting parameters  $a_1$ ,  $b_1$ ,  $a_2$ ,  $b_2$  are listed in Table 4 for  $\omega \in [0, 1]$ . Indeed, this elementary function gives an excellent approximation and the coefficient of determination for all  $\omega$  is  $R^2 = 1$ . Therefore, the fitting function in Eq. (100) with the parameters from Table 4 can be readily used as the basis for experimental analysis. Insensitivity of the force relaxation response to  $\omega$  means that these master curves can be a rather reliable means for determining diffusivity  $c$ , since the end result will not be much affected by the uncertainty in  $\omega$ . Consequently, for an arbitrary  $\omega$ , linear interpolation with the data in Table 4 can simply be used to find the fitting parameters.

A protocol of data interpretation for this type of indentation experiment can be established as follows. The two force asymptotes can be used to determine material constants  $G/\phi$ ,  $G(2\eta - 1)/\eta$  and the ratio of the two asymptotes gives constant  $\omega$ . Once  $\omega$  is known, hydraulic diffusivity  $c$  can be determined by matching

the transient force response with the fitting function  $f_n(t_*)$ . In addition, if the early and late time asymptotes can be clearly identified from the experimental data, the diffusion coefficient  $c$  can also be computed from  $t_{*0.5}$  via the fitting function,  $t_{*0.5} = 0.1304 - 0.05968\omega + 0.03869\omega^2 - 0.01278\omega^3$ .

## 8. Concluding remarks

A fully coupled poroelastic solution to the problem of spherical indentation in a semi-infinite domain with a fully drained surface via step displacement loading is presented in this work. The method of solution is based on the McNamee–Gibson displacement function method. We overcome the mathematical difficulties previously encountered in deriving theoretical solutions for poroelastic contact problems in the literature. Effective solution schemes for evaluating integrals with oscillatory kernels and for solving the Fredholm integral equation of the second kind are developed. Field quantities on the surface as well as inside the domain are both derived. Hydromechanical coupling in such an indentation process results in the Mandel–Cryer effect in the pore pressure distribution along the contact axis. Compared with the classical Hertzian contact, initiation of the cone and median cracks are more likely to occur as a result of the poroelastic effect.

Though derivation of this theoretical solution requires the aid of a variety of mathematical techniques, the result in terms of the normalized indentation force relaxation with time is remarkably simple. The transient force response shows only weak dependence on the material constant  $\omega$  and can be fitted by a four-parameter elementary function.

In principle, the force relaxation behavior can be used for material characterization in the laboratory. The asymptotes of the indentation force at the early and late times can be used to determine  $G/\phi$  and  $G(2\eta - 1)/\eta$ . The ratio between the two yields the constant  $\omega$ . Hydraulic diffusivity  $c$  can then be determined by matching the measured transient force response with the theoretical solution.

To fully develop this type of indentation experiments into a laboratory testing technique for materials such as rocks, potential complications from tensile fracturing and plastic deformation must be considered. Numerical analysis becomes necessary in order to identify the parameter range where the poroelastic solution is applicable. It is noted that although practically speaking, the loading rate in an experiment, whether by force- or displacement-controlled, is always finite, a theoretical solution assuming Heaviside step loading is an idealization which can serve as a bound for the finite loading rate cases (Galli and Oyen, 2009; Bouklas et al., 2015). Only the fully drained surface condition with step displacement loading is analyzed in the present work. Mixed drainage and undrained conditions as well as step force loading could be examined in the future.

## Acknowledgements

Partial financial support from the Sand Control Client Advisory Board of Schlumberger is gratefully acknowledged.

## Appendix A. Additional stress and displacement fields

In addition to the pore pressure and vertical stress and displacement fields in Section 5, here we provide the expressions for the remaining non-trivial stress and displacement fields in the Laplace domain and their asymptotes at the early and late times in the time domain. Similar to Section 5, two sets of expressions are provided for the field quantities.

## A1. Radial stress

### A1.1. Expression 1

$$\bar{\sigma}_r = \frac{2Ga^3}{c\phi R} \left\{ s_*^{-1} \int_0^1 (m_*^2 - 1) \left[ \begin{matrix} N_{sr1}(s_*, r_*, m_*, z_*) \\ + N_{sr2}(s_*, r_*, m_*, z_*) \end{matrix} \right] dm_* \right. \\ \left. + s_*^{-1} \int_1^\infty m_*^{\frac{1}{2}} \theta_1(s_*, m_*) \left[ \begin{matrix} N_{sr1}(s_*, r_*, m_*, z_*) \\ + N_{sr2}(s_*, r_*, m_*, z_*) \end{matrix} \right] dm_* \right\} \quad (A.1)$$

where,

$$N_{sr1}(s_*, r_*, m_*, z_*) \\ = \sqrt{\frac{2}{\pi}} m_*^{\frac{1}{2}} \int_0^\infty \xi_*^{\frac{3}{2}} \left\{ \frac{2\omega}{1+\omega} \left[ -s_*^{-1} \xi_* \sqrt{\xi_*^2 + s_*} \exp(-z_* \xi_*) \right. \right. \\ \left. \left. + (1 + s_*^{-1} \xi_*^2) \exp(-z_* \sqrt{\xi_*^2 + s_*}) \right] \right. \\ \left. + (z_* \xi_* - 1) \exp(-z_* \xi_*) \right\} J_{-\frac{1}{2}}(m_* \xi_*) J_0(r_* \xi_*) d\xi_* \quad (A.2)$$

$$N_{sr2}(s_*, r_*, m_*, z_*) \\ = \sqrt{\frac{2}{\pi}} m_*^{\frac{1}{2}} r_*^{-1} \int_0^\infty \xi_*^{\frac{1}{2}} \left\{ \frac{2\omega}{1+\omega} \left[ s_*^{-1} \xi_* \sqrt{\xi_*^2 + s_*} \exp(-z_* \xi_*) \right. \right. \\ \left. \left. - s_*^{-1} \xi_*^2 \exp(-z_* \sqrt{\xi_*^2 + s_*}) \right] \right. \\ \left. - (1 - \phi + z_* \xi_*) \exp(-z_* \xi_*) \right\} J_{-\frac{1}{2}}(m_* \xi_*) J_1(r_* \xi_*) d\xi_* \quad (A.3)$$

### A1.2. Expression 2

The second expression for  $\bar{\sigma}_r$  can be derived by decomposing  $\bar{\sigma}_r$  into  $\bar{\sigma}_r = \bar{\sigma}_{r1} + \bar{\sigma}_{r2}$ , where  $\bar{\sigma}_{r1}$  and  $\bar{\sigma}_{r2}$  correspond to the parts of the equation containing  $N_{sr1}$  and  $N_{sr2}$  in Eq. (A.1), respectively. Applying Eq. (26) to  $\bar{\sigma}_{r1}$ , we obtain,

$$\int_{x_*}^\infty \bar{\sigma}_{r1} r_* (r_*^2 - x_*^2)^{-\frac{1}{2}} dr_* \\ = \frac{2Ga^3}{c\phi R} \left[ s_*^{-1} \int_0^1 (m_*^2 - 1) N_{sr1}(s_*, x_*, m_*, z_*) dm_* \right. \\ \left. + s_*^{-1} \int_1^\infty m_*^{\frac{1}{2}} \theta_1(s_*, m_*) N_{sr1}(s_*, x_*, m_*, z_*) dm_* \right] \quad (A.4)$$

where,

$$N_{sr1}(s_*, x_*, m_*, z_*) \\ = \frac{2}{\pi} \int_0^\infty \left\{ \frac{2\omega}{1+\omega} \left[ -s_*^{-1} \xi_* \sqrt{\xi_*^2 + s_*} \exp(-z_* \xi_*) \right. \right. \\ \left. \left. + \exp(-z_* \sqrt{\xi_*^2 + s_*}) + s_*^{-1} \xi_*^2 \exp(-z_* \sqrt{\xi_*^2 + s_*}) \right] \right. \\ \left. + (z_* \xi_* - 1) \exp(-z_* \xi_*) \right\} \cos(m_* \xi_*) \cos(x_* \xi_*) d\xi_* \quad (A.5)$$

Applying Eq. (63) to  $\bar{\sigma}_{r2}$ , we have,

$$\int_{x_*}^\infty \bar{\sigma}_{r2} r_* (r_*^2 - x_*^2)^{-\frac{1}{2}} dr_* \\ = \frac{2Ga^3}{c\phi R} \left[ s_*^{-1} \int_0^1 (m_*^2 - 1) N_{sr2}(s_*, x_*, m_*, z_*) dm_* \right. \\ \left. + s_*^{-1} \int_1^\infty m_*^{\frac{1}{2}} \theta_1(s_*, m_*) N_{sr2}(s_*, x_*, m_*, z_*) dm_* \right] \quad (A.6)$$

where,

$$N_{sr2}(s_*, x_*, m_*, z_*) \\ = \frac{2}{\pi} x_*^{-1} \int_0^\infty \xi_*^{-1} \left\{ \frac{2\omega}{1+\omega} \left[ s_*^{-1} \xi_* \sqrt{\xi_*^2 + s_*} \exp(-z_* \xi_*) \right. \right. \\ \left. \left. - (2 - \phi) \exp(-z_* \xi_*) \right] \right\} J_{-\frac{1}{2}}(m_* \xi_*) J_0(r_* \xi_*) d\xi_*$$

$$\left. - s_*^{-1} \xi_*^2 \exp(-z_* \sqrt{\xi_*^2 + s_*}) \right] \\ - (1 - \phi + z_* \xi_*) \exp(-z_* \xi_*) \left\} \cos(m_* \xi_*) \sin(x_* \xi_*) d\xi_* \quad (A.7)$$

On the surface ( $z_* = 0$ ), Eq. (A.4) becomes,

$$\int_{x_*}^\infty \bar{\sigma}_{r1} r_* (r_*^2 - x_*^2)^{-\frac{1}{2}} dr_* = \int_{x_*}^\infty \bar{\sigma}_z r_* (r_*^2 - x_*^2)^{-\frac{1}{2}} dr_* \\ + \frac{2G(1 - 2\eta)a^3}{c\eta R} s_*^{-1} x_*^{\frac{1}{2}} \theta_1(s_*, x_*) \quad (A.8)$$

Applying the inverse Abel transform gives,

$$\bar{\sigma}_{r1} = \bar{\sigma}_z + \frac{4G(2\eta - 1)a^3}{\pi c\eta R} s_*^{-1} \int_{r_*}^\infty \theta_3(s_*, x_*) (x_*^2 - r_*^2)^{-\frac{1}{2}} dx_* \quad (A.9)$$

Similarly,  $\bar{\sigma}_{r2}$  can be expressed as follows, at  $r_* \leq 1$ ,

$$\bar{\sigma}_{r2} = -\frac{4Ga^3}{\pi c\phi R} s_*^{-1} \int_{r_*}^1 \left[ \begin{matrix} x_*^{-2} \theta_2(s_*, x_*) \\ + \left( \phi - \frac{1}{1+\omega} \right) x_*^{-1} (x_*^2 - 1) \\ + \frac{1}{1+\omega} x_*^{\frac{1}{2}} \theta_1(s_*, x_*) \end{matrix} \right] (x_*^2 - r_*^2)^{-\frac{1}{2}} dx_* \\ - \frac{4Ga^3}{\pi c\phi R} s_*^{-1} \int_1^\infty \left[ \begin{matrix} x_*^{-2} \theta_2(s_*, x_*) \\ + \phi x_*^{-\frac{1}{2}} \theta_1(s_*, x_*) \end{matrix} \right] (x_*^2 - r_*^2)^{-\frac{1}{2}} dx_* \quad (A.10)$$

and at  $r_* \geq 1$ ,

$$\bar{\sigma}_{r2} = -\frac{4Ga^3}{\pi c\phi R} s_*^{-1} \int_{r_*}^\infty \left[ \begin{matrix} x_*^{-2} \theta_2(s_*, x_*) \\ + \phi x_*^{-\frac{1}{2}} \theta_1(s_*, x_*) \end{matrix} \right] (x_*^2 - r_*^2)^{-\frac{1}{2}} dx_* \quad (A.11)$$

Expressions for  $\theta_2(s_*, x_*)$  and  $\theta_3(s_*, x_*)$  are given in Appendix C.

Inside the half space ( $z_* > 0$ ),

$$\bar{\sigma}_r = -\frac{4Ga^3}{\pi c\phi R} \int_{r_*}^\infty \theta_{sr}(s_*, x_*, z_*) (x_*^2 - r_*^2)^{-\frac{1}{2}} dx_* \quad (A.12)$$

where,

$$\theta_{sr}(s_*, x_*, z_*) = s_*^{-1} \int_0^1 (m_*^2 - 1) N_{srX}(s_*, x_*, m_*, z_*) dm_* \\ + s_*^{-1} \int_1^\infty m_*^{\frac{1}{2}} \theta_1(s_*, m_*) N_{srX}(s_*, x_*, m_*, z_*) dm_* \quad (A.13)$$

and  $N_{srX} = \partial(N_{sr1} + N_{sr2})/\partial x_*$ . The expression of  $N_{srX}$  and other similar derivatives from the sections below are omitted here.

## A2. Tangential stress

### A2.1. Expression 1

$$\bar{\sigma}_\theta = \frac{2Ga^3}{c\phi R} \left\{ s_*^{-1} \int_0^1 (m_*^2 - 1) \left[ \begin{matrix} N_{s\theta1}(s_*, r_*, m_*, z_*) \\ - N_{sr2}(s_*, r_*, m_*, z_*) \end{matrix} \right] dm_* \right. \\ \left. + s_*^{-1} \int_1^\infty m_*^{\frac{1}{2}} \theta_1(s_*, m_*) \left[ \begin{matrix} N_{s\theta1}(s_*, r_*, m_*, z_*) \\ - N_{sr2}(s_*, r_*, m_*, z_*) \end{matrix} \right] dm_* \right\} \quad (A.14)$$

where,

$$N_{s\theta1}(s_*, r_*, m_*, z_*) \\ = \sqrt{\frac{2}{\pi}} m_*^{\frac{1}{2}} \int_0^\infty \xi_*^{\frac{3}{2}} \left[ \frac{2\omega}{1+\omega} \exp(-z_* \sqrt{\xi_*^2 + s_*}) \right. \\ \left. - (2 - \phi) \exp(-z_* \xi_*) \right] J_{-\frac{1}{2}}(m_* \xi_*) J_0(r_* \xi_*) d\xi_* \quad (A.15)$$



### A2.2. Expression 2

Let  $\bar{\sigma}_\theta = \bar{\sigma}_{\theta 1} + \bar{\sigma}_{\theta 2}$ , where  $\bar{\sigma}_{\theta 1}$  and  $\bar{\sigma}_{\theta 2}$  are the parts of the equations containing  $N_{s\theta 1}$  and  $N_{sr2}$  in Eq. (A.14), respectively. We have  $\bar{\sigma}_{\theta 2} = -\bar{\sigma}_{r2}$ . Applying Eq. (26) to  $\bar{\sigma}_{\theta 1}$  gives,

$$\begin{aligned} & \int_{x_*}^{\infty} \bar{\sigma}_{\theta 1} r_* (r_*^2 - x_*^2)^{-\frac{1}{2}} dr_* \\ &= \frac{2Ga^3}{c\phi R} \left[ s_*^{-1} \int_0^1 (m_*^2 - 1) N_{s\theta 1}(s_*, x_*, m_*, z_*) dm_* \right. \\ & \quad \left. + s_*^{-1} \int_1^{\infty} m_*^{\frac{1}{2}} \theta_1(s_*, m_*) N_{s\theta 1}(s_*, x_*, m_*, z_*) dm_* \right] \end{aligned} \quad (\text{A.16})$$

where,

$$\begin{aligned} N_{s\theta 1}(s_*, x_*, m_*, z_*) \\ &= \frac{2}{\pi} \int_0^{\infty} \left[ \frac{2\omega}{1+\omega} \exp(-z_* \sqrt{\xi_*^2 + s_*}) \right. \\ & \quad \left. - (2 - \phi) \exp(-z_* \xi_*) \right] \cos(m_* \xi_*) \cos(x_* \xi_*) d\xi_* \end{aligned} \quad (\text{A.17})$$

On the surface ( $z_* = 0$ ), Eq. (A.16) becomes,

$$\begin{aligned} & \int_{x_*}^{\infty} \bar{\sigma}_{\theta 1} r_* (r_*^2 - x_*^2)^{-\frac{1}{2}} dr_* \\ &= \frac{2 - 2\eta}{1 - 2\eta} \int_{x_*}^{\infty} \bar{\sigma}_{r2} r_* (r_*^2 - x_*^2)^{-\frac{1}{2}} dr_* \\ & \quad + \frac{2G(1 - \eta)a^3}{c\eta R} s_*^{-1} x_*^{\frac{1}{2}} \theta_1(s_*, x_*) \end{aligned} \quad (\text{A.18})$$

Applying the inverse Abel transform gives,

$$\bar{\sigma}_{\theta 1} = \frac{2 - 2\eta}{1 - 2\eta} \bar{\sigma}_z + \frac{4G(\eta - 1)a^3}{\pi c\eta R} s_*^{-1} \int_{r_*}^{\infty} \theta_3(s_*, x_*) (x_*^2 - r_*^2)^{-\frac{1}{2}} dx_* \quad (\text{A.19})$$

Inside the half space ( $z_* > 0$ ),

$$\bar{\sigma}_\theta = -\frac{4Ga^3}{\pi c\phi R} \int_{r_*}^{\infty} \theta_{s\theta}(s_*, x_*, z_*) (x_*^2 - r_*^2)^{-\frac{1}{2}} dx_* \quad (\text{A.20})$$

where,

$$\begin{aligned} \theta_{s\theta}(s_*, x_*, z_*) &= s_*^{-1} \int_0^1 (m_*^2 - 1) N_{s\theta X, X}(s_*, x_*, m_*, z_*) dm_* \\ & \quad + s_*^{-1} \int_1^{\infty} m_*^{\frac{1}{2}} \theta_1(s_*, m_*) N_{s\theta X, X}(s_*, x_*, m_*, z_*) dm_* \end{aligned} \quad (\text{A.21})$$

and  $N_{s\theta X, X} = \partial(N_{s\theta 1} - N_{sr2})/\partial x_*$ .

### A3. Shear stress

#### A3.1. Expression 1

$$\begin{aligned} \bar{\sigma}_{zr} &= \frac{2Ga^3}{c\phi R} \left[ s_*^{-1} \int_0^1 (m_*^2 - 1) N_{s2r}(s_*, r_*, m_*, z_*) dm_* \right. \\ & \quad \left. + s_*^{-1} \int_1^{\infty} m_*^{\frac{1}{2}} \theta_1(s_*, m_*) N_{s2r}(s_*, r_*, m_*, z_*) dm_* \right] \end{aligned} \quad (\text{A.22})$$

where,

$$\begin{aligned} N_{s2r}(s_*, r_*, m_*, z_*) \\ &= \sqrt{\frac{2}{\pi}} m_*^{\frac{1}{2}} \int_0^{\infty} \xi_*^{\frac{3}{2}} \left[ \frac{2\omega}{1+\omega} s_*^{-1} \xi_* \sqrt{\xi_*^2 + s_*} \exp(-z_* \xi_*) \right. \\ & \quad \left. - \frac{2\omega}{1+\omega} s_*^{-1} \xi_* \sqrt{\xi_*^2 + s_*} \exp(-z_* \sqrt{\xi_*^2 + s_*}) \right. \\ & \quad \left. - z_* \xi_* \exp(-z_* \xi_*) \right] J_{-\frac{1}{2}}(m_* \xi_*) J_1(r_* \xi_*) d\xi_* \end{aligned} \quad (\text{A.23})$$

### A3.2. Expression 2

Applying Eq. (63) to Eq. (A.22) gives,

$$\begin{aligned} & \int_{x_*}^{\infty} \bar{\sigma}_{zr} (r_*^2 - x_*^2)^{-\frac{1}{2}} dr_* \\ &= \frac{2Ga^3}{c\phi R} \left[ s_*^{-1} \int_0^1 (m_*^2 - 1) N_{s2rX}(s_*, x_*, m_*, z_*) dm_* \right. \\ & \quad \left. + s_*^{-1} \int_1^{\infty} m_*^{\frac{1}{2}} \theta_1(s_*, m_*) N_{s2rX}(s_*, x_*, m_*, z_*) dm_* \right] \end{aligned} \quad (\text{A.24})$$

where,

$$\begin{aligned} N_{s2rX}(s_*, x_*, m_*, z_*) \\ &= \frac{2}{\pi} x_*^{-1} \int_0^{\infty} \left[ \frac{2\omega}{1+\omega} s_*^{-1} \xi_* \sqrt{\xi_*^2 + s_*} \exp(-z_* \xi_*) \right. \\ & \quad \left. - \frac{2\omega}{1+\omega} s_*^{-1} \xi_* \sqrt{\xi_*^2 + s_*} \exp(-z_* \sqrt{\xi_*^2 + s_*}) \right. \\ & \quad \left. - z_* \xi_* \exp(-z_* \xi_*) \right] \cos(m_* \xi_*) \sin(x_* \xi_*) d\xi_* \end{aligned} \quad (\text{A.25})$$

Inside the domain ( $z_* > 0$ ), applying Eq. (61) to Eq. (A.24) gives the shear stress in the Laplace domain,

$$\bar{\sigma}_{zr} = -\frac{4Ga^3}{\pi c\phi R} r_* \int_{r_*}^{\infty} \theta_{s2r}(s_*, x_*, z_*) (x_*^2 - r_*^2)^{-\frac{1}{2}} dx_* \quad (\text{A.26})$$

where,

$$\begin{aligned} \theta_{s2r}(s_*, x_*, z_*) &= s_*^{-1} \int_0^1 (m_*^2 - 1) N_{s2rX, X}(s_*, x_*, m_*, z_*) dm_* \\ & \quad + s_*^{-1} \int_1^{\infty} m_*^{\frac{1}{2}} \theta_1(s_*, m_*) N_{s2rX, X}(s_*, x_*, m_*, z_*) dm_* \end{aligned} \quad (\text{A.27})$$

and  $N_{s2rX, X} = \partial N_{s2rX}/\partial x_*$ .

### A4. Radial displacement

#### A4.1. Expression 1

$$\begin{aligned} \bar{u}_r &= \frac{a^4}{c\phi R} \left[ s_*^{-1} \int_0^1 (m_*^2 - 1) N_{ur}(s_*, r_*, m_*, z_*) dm_* \right. \\ & \quad \left. + s_*^{-1} \int_1^{\infty} m_*^{\frac{1}{2}} \theta_1(s_*, m_*) N_{ur}(s_*, r_*, m_*, z_*) dm_* \right] \end{aligned} \quad (\text{A.28})$$

where,

$$\begin{aligned} N_{ur}(s_*, r_*, m_*, z_*) \\ &= \sqrt{\frac{2}{\pi}} m_*^{\frac{1}{2}} \int_0^{\infty} \xi_*^{\frac{1}{2}} \left\{ \frac{2\omega}{1+\omega} s_*^{-1} \xi_* \sqrt{\xi_*^2 + s_*} \exp(-z_* \xi_*) \right. \\ & \quad \left. - s_*^{-1} \xi_*^2 \exp(-z_* \sqrt{\xi_*^2 + s_*}) \right\} \\ & \quad \left. - (1 - \phi + z_* \xi_*) \exp(-z_* \xi_*) \right\} J_{-\frac{1}{2}}(m_* \xi_*) J_1(r_* \xi_*) d\xi_* \end{aligned} \quad (\text{A.29})$$

#### A4.2. Expression 2

Since  $N_{ur} = r_* N_{sr2}$ , the second expression for  $\bar{u}_r$  can be derived based on the treatment for Eq. (A.3) in A.1.

**Table A1**

Early time asymptotes of the poroelastic fields.

Early time asymptotes ( $t \rightarrow 0$ )	
$\alpha p$	$\frac{4\eta\omega Ga}{\phi(1+\omega)R} \int_0^1 (1-m_*^2) I_2 dm_*$
$\sigma_z$	$\frac{2Ga}{\phi R} \int_0^1 (1-m_*^2) (I_2 + z_* I_3) dm_*$
$\sigma_r$	$\frac{2Ga}{\phi R} \int_0^1 (1-m_*^2) [I_2 - z_* I_3 + (1-\phi)I_4 + z_* I_5] dm_*$
$\sigma_\theta$	$-\frac{2Ga}{\phi R} \int_0^1 (1-m_*^2) [(\phi-2)I_2 + (1-\phi)I_4 + z_* I_5] dm_*$
$\sigma_{zr}$	$\frac{2Ga}{\phi R} r_* z_* \int_0^1 (1-m_*^2) I_6 dm_*$
$u_z$	$\frac{a^2}{\phi R} \int_0^1 (1-m_*^2) (\phi I_1 + z_* I_2) dm_*$
$u_r$	$\frac{a^2}{\phi R} r_* \int_0^1 (1-m_*^2) [(1-\phi)I_4 + z_* I_5] dm_*$

**Table A2**

Late time asymptotes of the poroelastic fields.

Late time asymptotes ( $t \rightarrow \infty$ )	
$\alpha p$	0
$\sigma_z$	$\frac{G(2\eta-1)a}{\eta R} \int_0^1 (1-m_*^2) (I_2 + z_* I_3) dm_*$
$\sigma_r$	$\frac{G(2\eta-1)a}{\eta R} \int_0^1 (1-m_*^2) \left( I_2 - z_* I_3 + \frac{1}{1-2\eta} I_4 + z_* I_5 \right) dm_*$
$\sigma_\theta$	$-\frac{Ga}{\eta R} \int_0^1 (1-m_*^2) [(2-2\eta)I_2 - I_4 + (2\eta-1)z_* I_5] dm_*$
$\sigma_{zr}$	$\frac{G(2\eta-1)a}{\eta R} r_* z_* \int_0^1 (1-m_*^2) I_6 dm_*$
$u_z$	$\frac{a^2}{R} \int_0^1 (1-m_*^2) \left[ I_1 - \left( \frac{1-2\eta}{2\eta} \right) z_* I_2 \right] dm_*$
$u_r$	$-\frac{a^2}{2R} r_* \int_0^1 (1-m_*^2) \left[ \frac{1}{\eta} I_4 + \left( \frac{1-2\eta}{\eta} \right) z_* I_5 \right] dm_*$

#### A5. Early and late time asymptotes

### Appendix B. Contour integration

The application of the method of contour integration for rewriting an integral with an oscillatory kernel is illustrated here. For example, the first term in Eq. (79) can be written in form of,

$$\int_0^\infty \xi_*^2 \sqrt{\xi_*^2 + s_*} \exp(-z_* \xi_*) \sin(y \xi_*) d\xi_* \quad (\text{B.1})$$

This is the imaginary part of,

$$\int_0^\infty \xi_*^2 \sqrt{\xi_*^2 + s_*} \exp[-(z_* + iy) \xi_*] d\xi_* \quad (\text{B.2})$$

Since the integrand in Eq. (B.2) is analytical inside the domain enclosed by the contour  $C_1 + C_2 + C_3$ , see Fig. B.15, integration along the closed contour should be zero. In addition, according to Jordan's lemma, the integral over the circular arc  $C_2$  does not contribute. Therefore, the integral along  $C_1$  (Eq. (B.2)) equals to the negative value of the integral along path  $C_3$ ,

$$-\int_{C_3} \xi_*^2 \sqrt{\xi_*^2 + s_*} \exp[-(z_* + iy) \xi_*] d\xi_* \quad (\text{B.3})$$

Path  $C_3$  can be parameterized as  $\xi_* = (z_* - iy) \xi_*$ . Eq. (B.3) then becomes,

$$(iy - z_*)^3 \int_0^\infty \xi_*^2 \sqrt{(z_* - iy)^2 \xi_*^2 + s_*} \exp[-(z_*^2 + y^2) \xi_*] d\xi_* \quad (\text{B.4})$$

**Table A3**

Expressions of  $I_1(z_*, m_*, r_*) - I_6(z_*, m_*, r_*)$ .

$I_1$	$\frac{2}{\pi} \int_0^\infty \exp(-z_* \xi_*) \cos(m_* \xi_*) J_0(r_* \xi_*) d\xi_*$ $= \frac{2}{\pi} \text{Re} \left\{ [(z_* + im_*)^2 + r_*^2]^{-\frac{1}{2}} \right\}$
$I_2$	$\frac{2}{\pi} \int_0^\infty \xi_* \exp(-z_* \xi_*) \cos(m_* \xi_*) J_0(r_* \xi_*) d\xi_*$ $= \frac{2}{\pi} \text{Re} \left\{ (z_* + im_*) [(z_* + im_*)^2 + r_*^2]^{-\frac{3}{2}} \right\}$
$I_3$	$\frac{2}{\pi} \int_0^\infty \xi_*^2 \exp(-z_* \xi_*) \cos(m_* \xi_*) J_0(r_* \xi_*) d\xi_*$ $= \frac{2}{\pi} \text{Re} \left\{ 3(z_* + im_*)^2 [(z_* + im_*)^2 + r_*^2]^{-\frac{5}{2}} \right\}$
$I_4$	$\frac{2}{\pi r_*} \int_0^\infty \exp(-z_* \xi_*) \cos(m_* \xi_*) J_1(r_* \xi_*) d\xi_*$ $= \frac{2}{\pi r_*^2} \text{Re} \left\{ 1 - (z_* + im_*) [(z_* + im_*)^2 + r_*^2]^{-\frac{1}{2}} \right\}$
$I_5$	$\frac{2}{\pi r_*} \int_0^\infty \xi_* \exp(-z_* \xi_*) \cos(m_* \xi_*) J_1(r_* \xi_*) d\xi_*$ $= \frac{2}{\pi} \text{Re} \left\{ [(z_* + im_*)^2 + r_*^2]^{-\frac{3}{2}} \right\}$
$I_6$	$\frac{2}{\pi r_*} \int_0^\infty \xi_*^2 \exp(-z_* \xi_*) \cos(m_* \xi_*) J_1(r_* \xi_*) d\xi_*$ $= \frac{2}{\pi} \text{Re} \left\{ 3(z_* + im_*) [(z_* + im_*)^2 + r_*^2]^{-\frac{3}{2}} \right\}$

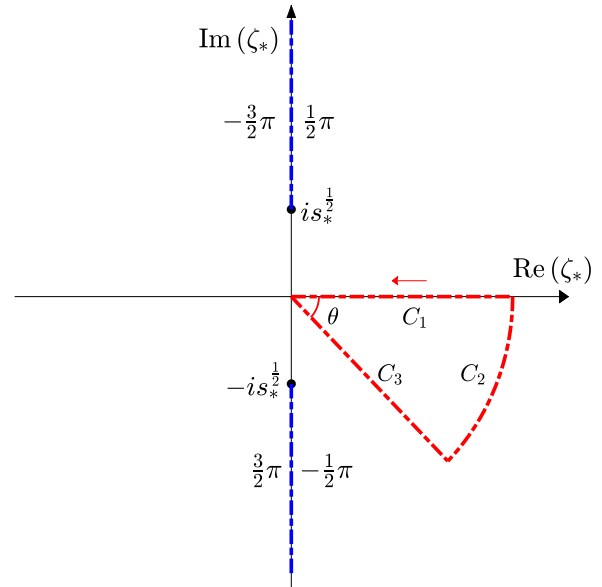


**Fig. B.15.** Integration contour (red dashed lines) and branch cuts (blue dashed lines) in the complex plane. In the contour,  $\theta = \arctan(y/z_*)$ ;  $C_1$  is the path from  $\infty$  to 0 in the negative direction of the real axis;  $C_3$  is a ray with an argument of  $-\theta$ ; and  $C_2$  is a circular arc connecting the end point of path  $C_3$  to the starting point of path  $C_1$ .

Thus, Eq. (B.1) equals to the imaginary part of Eq. (B.4), where the oscillatory nature is no longer present.

### Appendix C. Expressions for $\theta_2(s, x)$ and $\theta_3(s, x)$

Functions  $\theta_2(s, x)$  and  $\theta_3(s, x)$  can be evaluated from direct integration of the following integrals.

$$\theta_2(s, x) = \int_0^1 (m^2 - 1) N_2(s, x, m) dm + \int_1^\infty m^{\frac{1}{2}} \theta_1(s, m) N_2(s, x, m) dm \quad (\text{C.1})$$

where,

$$N_2(s, x, m) = \left( \frac{\omega}{1+\omega} \right) s^{-\frac{1}{2}} \left[ (x-m)^{-1} M_1 \left( |x-m| s^{\frac{1}{2}} \right) + (x+m)^{-1} M_1 \left( (x+m) s^{\frac{1}{2}} \right) \right] + (1-\phi) \mathbb{H}(x-m) \quad (C.2)$$

And,

$$\theta_3(s, x) = \omega \int_0^1 (m^2 - 1) N_3(s, x, m) dm + \omega \int_1^\infty m^{\frac{1}{2}} \theta_1(s, m) N_3(s, x, m) dm \quad (C.3)$$

where,

$$N_3(s, x, m) = (x-m)^{-1} s^{\frac{1}{2}} \left\{ -\frac{2}{\pi} + 3|x-m|^{-1} s^{-\frac{1}{2}} M_0 \left( |x-m| s^{\frac{1}{2}} \right) - \left[ 1 + 6(x-m)^{-2} s^{-1} \right] M_1 \left( |x-m| s^{\frac{1}{2}} \right) \right\} + (x+m)^{-1} s^{\frac{1}{2}} \left\{ -\frac{2}{\pi} + 3(x+m)^{-1} s^{-\frac{1}{2}} M_0 \left( (x+m) s^{\frac{1}{2}} \right) - \left[ 1 + 6(x+m)^{-2} s^{-1} \right] M_1 \left( (x+m) s^{\frac{1}{2}} \right) \right\} \quad (C.4)$$

## References

- Agbezuge, L.K., Deresiewicz, H., 1974. On the indentation of a consolidating half-space. *Israel J. Technol.* 12, 322–338.
- Argatov, I., Mishuris, G., 2018. *Indentation Testing of Biological Materials*. Springer.
- Bateman, H., 1954. *Tables of Integral Transforms*. McGraw-Hill.
- Biot, M., 1941. General theory of three-dimensional consolidation. *J. Appl. Phys.* 12, 155–164.
- Bouklas, N., Landis, C.M., Huang, R., 2015. A nonlinear, transient finite element method for coupled solvent diffusion and large deformation of hydrogels. *J. Mech. Phys. Solids* 79, 21–43.
- Bracewell, R.N., 1986. *The Fourier Transform and its Applications*. McGraw-Hill New York.
- Cheng, A.H.-D., 2016. *Poroelectricity*, 27. Springer.
- Chiarella, C., Booker, J.R., 1975. The time-settlement behaviour of a rigid die resting on a deep clay layer. *Q. J. Mech. Appl. Math.* 28 (3), 317–328.
- Cook, N.G.W., Hood, M., Tsai, F., 1984. Observations of crack growth in hard rock loaded by an indenter. In: *International Journal of Rock Mechanics and Mining Sciences & Geomechanics Abstracts*, 21. Elsevier, pp. 97–107.
- Cook, R.F., Pharr, G.M., 1990. Direct observation and analysis of indentation cracking in glasses and ceramics. *J. Am. Ceram. Soc.* 73 (4), 787–817.
- Deresiewicz, H., 1979. Effects of restricted flow at the surface of saturated clay. *Int. J. Numer. Anal. Methods Geomech.* 3 (1), 1–11.
- Detournay, E., Cheng, A.H.-D., 1993. *Comprehensive Rock Engineering*, 2. Pergamon, New York, pp. 113–171.
- Fowell, R.J., 1993. *Comprehensive Rock Engineering*, 4. Pergamon, Oxford, pp. 155–176.
- Galli, M., Oyen, M.L., 2008. Spherical indentation of a finite poroelastic coating. *Appl. Phys. Lett.* 93 (3), 031911.
- Galli, M., Oyen, M.L., 2009. Fast identification of poroelastic parameters from indentation tests. *Comput. Model. Eng. Sci.* 48 (3), 241–269.
- Hu, Y., Chan, E.P., Vlassak, J.J., Suo, Z., 2011a. Poroelastic relaxation indentation of thin layers of gels. *J. Appl. Phys.* 110, 086103.
- Hu, Y., Chen, X., Whitesides, G.M., Vlassak, J.J., Suo, Z., 2011b. Indentation of polydimethylsiloxane submerged in organic solvents. *J. Mater. Res.* 26 (6), 785–795.
- Hu, Y., You, J.-O., Auguste, D.T., Suo, Z., Vlassak, J.J., 2012. Indentation: a simple, non-destructive method for characterizing the mechanical and transport properties of pH-sensitive hydrogels. *J. Mater. Res.* 27 (1), 152–160.
- Hu, Y., Zhao, X., Vlassak, J.J., Suo, Z., 2010. Using indentation to characterize the poroelasticity of gels. *Appl. Phys. Lett.* 96 (12), 121904.
- Hui, C.-Y., Lin, Y.Y., Chuang, F.-C., Shull, K.R., Lin, W.-C., 2006. A contact mechanics method for characterizing the elastic properties and permeability of gels. *J. Polym. Sci. Part B* 44 (2), 359–370.
- Johnson, K.L., 1987. *Contact Mechanics*. Cambridge University Press.
- Kalcioglu, Z.I., Mahmoodian, R., Hu, Y., Suo, Z., Van Vliet, K.J., 2012. From macro-to microscale poroelastic characterization of polymeric hydrogels via indentation. *Soft Matter* 8 (12), 3393–3398.
- Kim, J., Selvadurai, A.P.S., 2016. A note on the consolidation settlement of a rigid circular foundation on a poroelastic halfspace. *Int. J. Numer. Anal. Methods Geomech.* 40 (14), 2003–2016.
- Lai, Y., Hu, Y., 2017. Unified solution for poroelastic oscillation indentation on gels for spherical, conical and cylindrical indenters. *Soft Matter* 13 (4), 852–861.
- Lan, Q., Selvadurai, A.P.S., 1996. Interacting indentors on a poroelastic half-space. *Zeitschrift für angewandte Mathematik und Physik ZAMP* 47 (5), 695–716.
- Lawn, B.R., 1998. Indentation of ceramics with spheres: a century after Hertz. *J. Am. Ceram. Soc.* 81 (8), 1977–1994.
- Lin, W.-C., Shull, K.R., Hui, C.-Y., Lin, Y.-Y., 2007. Contact measurement of internal fluid flow within poly(n-isopropylacrylamide) gels. *J. Chem. Phys.* 127 (9), 094906.
- Lin, Y.-Y., Hu, B.-W., 2006. Load relaxation of a flat rigid circular indenter on a gel half space. *J. Non-Cryst. Solids* 352 (38–39), 4034–4040.
- Liu, M., Huang, H., 2016. Sphere indentation - the Hertzian stress field and the effect of far-field confining stress. 50th US Rock Mechanics/Geomechanics Symposium. American Rock Mechanics Association.
- Love, A.E.H., 1929. The stress produced in a semi-infinite solid by pressure on part of the boundary. *Philos. Trans. R. Soc. London A* 228 (659–669), 377–420.
- Marshall, D.B., Cook, R.F., Padture, N.P., Oyen, M.L., Pajares, A., Bradby, J.E., Reimanis, I.E., Tandon, R., Page, T.F., Pharr, G.M., Law, B.R., 2015. The compelling case for indentation as a functional exploratory and characterization tool. *J. Am. Ceram. Soc.* 98 (9), 2671–2680.
- McNamee, J., Gibson, R.E., 1960a. Displacement functions and linear transforms applied to diffusion through porous elastic media. *Q. J. Mech. Appl. Math.* 13 (1), 98–111.
- McNamee, J., Gibson, R.E., 1960b. Plane strain and axially symmetric problems of the consolidation of a semi-infinite clay stratum. *Q. J. Mech. Appl. Math.* 13 (2), 210–227.
- Noble, B., 1963. The solution of Bessel function dual integral equations by a multiplying-factor method. *Math. Proc. Cambridge Philos. Soc.* 59 (2), 351–362.
- Olver, F.W.J., Lozier, D.W., Boisvert, R.F., Clark, C.W., 2010. *NIST Handbook of Mathematical Functions*. Cambridge University Press.
- Oyen, M.L., 2008. Poroelastic nanoindentation responses of hydrated bone. *J. Mater. Res.* 23 (5), 1307–1314.
- Rice, J.R., Cleary, M.P., 1976. Some basic stress diffusion solutions for fluid-saturated elastic porous media with compressible constituents. *Rev. Geophys.* 14 (2), 227–241.
- Stehfest, H., 1970. Algorithm 368: numerical inversion of Laplace transforms. *Commun. ACM* 13 (1), 47–49.
- Terzaghi, K., 1943. *Theoretical Soil Mechanics*. John Wiley & Sons, Inc.
- Verruijt, A., 2013. *Theory and Problems of Poroelasticity*. Delft University of Technology.
- Wang, H., 2000. *Theory of Linear Poroelasticity with Applications to Geomechanics and Hydrogeology*. Princeton University Press.
- Wynn, P., 1956. On a device for computing the  $e_m(s_n)$  transformation. *Mathematical Tables and Other Aids to Computation* 91–96.
- Yue, Z.Q., Selvadurai, A.P.S., 1995. Contact problem for saturated poroelastic solid. *J. Eng. Mech.* 121 (4), 502–512.
- Zemlyan, S.M., 2012. *The Classical Theory of Integral Equations: A Concise Treatment*. Springer.